Contents lists available at ScienceDirect

International Journal of Mechanical Sciences

journal homepage: www.elsevier.com/locate/ijmecsci

Two new hybrid methods in integrating constitutive equations

CrossMark

Mohammad Rezaiee-Pajand *, Mehrdad Sharifian, Mehrzad Sharifian

Ferdowsi University of Mashhad, Iran

A R T I C L E   I N F O

A B S T R A C T

It is crucial that more powerful integrations be developed as the plasticity models become more sophisticated. Here, two new robust integrating tactics are suggested based on the Exponential map and Euler's algorithms. The integrations are developed for the Drucker–Prager plasticity with nonlinear mixed hardening. Moreover, two different types of exponential strategies are advanced for the plasticity to be compared to the proposed techniques. Dealing with the apex of the yield surface is generally discussed for the integrations as well. Eventually, the proposed algorithms are thoroughly examined in a broad set of numerical tests comprising accuracy, efficiency, and convergence rate investigations. The results demonstrate the supremacy of the suggested schemes amid the six diverse techniques under discussion.

© 2013 Elsevier Ltd. All rights reserved.

1. Introduction

Whenever a material undergoes a plastic deformation, the corresponding constitutive equations are path-dependent and as a result the stress tensor is contingent upon the strain history as well as function of the instantaneous amount of the strain. Assuming a general path-dependent plasticity model, integration of rate constitutive equations offers the updated stresses whose strain histories are produced in the iterative solution of the equilibrium equations during a generic nonlinear finite element analysis. As an essential necessity to the finite element simulation of path-dependent problems, an appropriate technique for integrating a constitutive law is of great significance due to being dramatically in touch with the final results of the numerical analysis.

The history of incremental theory of plasticity and the integration of elastoplastic constitutive equations, as an inseparable part of it, have their roots many years ago [1]. However, the current form of the most well-known integrating technique is initially attributed to Wilkins [2]. Having clearly explained the procedure of an entire elastoplastic analysis, he formulated the equation of State for two phases of elastic and plastic flow regions and introduced the radial return algorithm to update the stress tensor at elastoplastic state such that the yield strength of the material is not exceeded. His integration technique was pragmatically used by Rice and Tracy [3] to study the elastic perfectly plastic state of

crack tip deformation by a finite element procedure. Later on, Krieg and Key [4] updated the algorithm for a more sophisticated plasticity to account for the isotropic and kinematic hardenings. Proposing an exact solution for perfect plasticity, Krieg and Krieg [5] are known as the frontiers of exact integrations. They also introduced the iso-error maps as a robust tool for examining the integrating tactics. Subsequently, Schreyer et al. [6] extended their scheme for a plasticity model with hardenings. At this point, it was time for a thorough investigation on the different integration schemes proposed to that time. Yoder and Whirley [7] performed a comparative examination which proved the general primacy of radial return integration, especially in the presence of hardening plasticity. Ortiz and Popov [8] extended the investigation on the ground of stability, likewise accuracy, to demonstrate the superior stability of the generalized midpoint over trapezoidal rules. An important fact of any of integration strategies is the consistent elastoplastic tangent modulus which is responsible for preserving the asymptotic rate of quadratic convergence in implicit finite element codes. The concept was first perceived by Nagtegaal [9] to which Simo and Taylor [10,11] and Dodds [12] are also known as pioneers. Meanwhile, Loret and Prevost [13] developed an exact solution for non-associative Drucker–Prager plasticity with linear isotropic hardening. After a brief review of new developments to that time, Runesson et al. [14] performed a comparison between midpoint and closest point integrations with respect to the treatment of non-smooth yield surfaces. Subsequently, Sloan and Booker [15] suggested that the constitutive equations of a non-smooth yield convex set such as Tresca or Mohr–Coulomb could be integrated exactly under certain circumstances. Afterwards, Genna and Pandolfi [16] illustrated a general two-step integration tactic

---

* Corresponding author. Tel.: +98 915 3130340; fax: +98 511 8412912.
  E-mail addresses: mrpajand@yahoo.com, rezaiee@um.ac.ir (M. Rezaiee-Pajand).

for the associative rate plasticity of Drucker–Prager model with some advantages over the typical radial return algorithm. At this point, Hopperstad and Remseth [17] came by a modified return mapping algorithm that would employ the closest point algorithm along with a decomposition method to achieve a more efficient integration. The last major attempt to improve the integration schemes in twentieth century was carried out by Wei et al. [18] where they proposed a consistent algorithm based on Prandtl–Reuss elastoplastic models combining the advantages of exact time integration of constitutive equations and the quadratic asymptotic convergence of Newton–Raphson iterative procedures.

In the past century, as reviewed, the researches in this field were chiefly to develop the implicit group of integrations such as closest point, midpoint, trapezoidal and so on, which uses the unknown values of the variables at each load increment and leads to an iterative process in the heart of their algorithms. These studies were followed by Kobayashi and Ohno [19] and Kobayashi et al. [20] where they executed an integration strategy based on closest point method for a cyclic plasticity and presented an implicit method for time-and-temperature dependent constitutive equations. Afterwards, Clausen et al. [21] presented a new return method based on the constant gradient of linear isotropic yield criteria achieving simple formulae with closed form solution and no iteration for such criteria. Similarly, Kan et al. [22] proposed another implicit integration based on the radial return method and Backward Euler's integration. Coombs et al. [23] offered an alternative to the Drucker–Prager and Mohr–Coulomb models by a conical surface with modified Reuleaux deviatoric sections, which presents a better accuracy in stress updating with Backward Euler approach.

On the other side, there are explicit integrations to which there is no iterative part to update the stress state since they obtain the variables utilizing the known values of the preceding load step. In the recent century, this sort of integrations found a new life via inaugurating a new technique called Exponential Map integration. In essence, the strategy is based on converting the constitutive equations of a given plasticity into the compact form of $\dot{\mathbf{X}} = \mathbb{A}\mathbf{X}$, which was originally addressed by Hong and Liu [24–26]. Inspired by the notion, Auricchio and Beirao da Veiga [27] are regarded as the founders who practically presented an exponential-based algorithm for integrating the constitutive equations of von-Mises plasticity with linear mixed hardening. Subsequently, Artioli et al. [28] modified their algorithm to be consistent with the yield surface. Liu [29–31] investigated the internal symmetries of the elastic perfectly plastic Drucker–Prager model and developed two exponential-based integration schemes. Later on, accuracy and convergence rate of the method were improved by Artioli et al. [32,33] and Rezaiee Pajand and Nasirai [34,35]. Afterwards, Rezaiee Pajand et al. [36,37] demonstrated the application of exponential-based integrations for a class of von-Mises plasticity with nonlinear isotropic and kinematic hardenings. Their methods were all fast and consistent having a considerable accuracy and efficiency for the considered plasticity models.

Besides, there is another general category of explicit integrations where the constitutive equations are directly integrated by an explicit Runge–Kutta technique such as Forward Euler, 2-stage RK method of order 2. Of the most recent efforts in this field one could find Sloan et al. [38] and Solowski and Gallipoli [39] helpful. It is also possible to reduce the number of constitutive equations to fewer ODEs and then hire the explicit Runge–Kutta techniques for solving them. Many studies have been performed in this area from which Wallin and Ristinmma [40,41], Szabo [42], Kossa and Szabo [43] and Rezaiee Pajand and Sharifian [44] are the most notable ones in the recent century.

In this study, two robust hybrid schemes are proposed established upon three major integrations of Exponential map, Backward Euler, and Forward Euler. The new algorithms could easily handle sophisticated plasticity models where the aforementioned tactics unveil their weak spots. The Drucker–Prager yield criterion along with nonlinear isotropic and kinematic hardenings is chosen as the plasticity to generally develop the integrations and also challenge their capabilities. Coping with the apex of the yield surface is described for the two general approaches of explicit and implicit integrations, as well. Moreover, the exponential map algorithm, and also Eulers' are derived for the plasticity model, which in case of the exponential map is totally new concerning the plasticity. Eventually, in a comprehensive numerical examination, the suggested schemes are thoroughly investigated. First, the accuracy is scrutinized by means of strain histories and iso-error maps. Second, the efficiencies are inspected via putting the computational effort versus the accuracy. And third, using the stress relative errors for a succession of load-step increments, the convergence rates of the schemes are verified. In all numerical tests, the results are compared to those of the exponential and Eulers' to clearly demonstrate the great accuracy and efficiency of the suggested algorithms.

2. Constitutive models

To broadly develop the new hybrid techniques, a generic constitutive model is taken into account where the Drucker–Prager yield surface [45] represents a pressure dependent plasticity alongside nonlinear mixed hardening. Many other plasticity models could be particularized from this generic state. Small deformation realm is also assumed for the strains. The following is the yield function proceeded by Chaboche's nonlinear mixed hardening:

$$F = \frac{1}{2}\mathbf{s}'^{\mathrm{T}}\mathbf{s}' - (\tau_y - \beta p')^2 = 0, \quad \tau_y - \beta p' > 0 \tag{1}$$

$$\dot{\tau}_y = \overline{b}(\tau_{y,0} + \tau_{y,s} - \tau_y)\dot{\gamma} \tag{2}$$

$$\dot{\mathbf{a}} = \sum_{i=1}^{m} \dot{\mathbf{a}}_i, \quad \dot{\mathbf{a}}_i = H_{\mathrm{kin},i}\dot{\mathbf{e}}^{\mathrm{p}} - H_{\mathrm{nl},i}\dot{\gamma}\mathbf{a}_i \tag{3}$$

Eqs. (2) and (3) display, respectively, the nonlinear isotropic and kinematic hardenings where τ_y is the yield stress in pure shear, $\tau_{y,0}$ is the initial pure shear stress, and $\tau_{y,s}$, $\overline{b}$, $H_{\mathrm{kin},i}$, and $H_{\mathrm{nl},i}$ are all material constants. For more in this, refer to Chaboche et al. [46], Chaboche [47,48] and Rezaiee-Pajand and Sinaie [49]. These hardening rules are the most applicable laws for regulating the yield surface evolution in nonlinear plasticity since they are quite capable of taking account of the transient stress–strain behavior of material and the ratcheting. Other parameters used in these relationships are all based on prevailing plasticity notation where a total stress is decomposed into its elements of shifted stress, σ', and back stress, $\mathbf{a}$:

$$\sigma = \sigma' + \mathbf{a} \tag{4}$$

The parameters $\mathbf{s}'$ and p' are, respectively, the deviatoric and hydrostatic/volumetric parts of the shifted stress:

$$\sigma' = \mathbf{s}' + p'\mathbf{i} \quad \text{with} \quad p' = \frac{\mathrm{tr}(\sigma')}{3} \tag{5}$$

The presence of the Kinematic hardening means the existence of the back stress as it determines the yield surface center when its location is going to change. Analogous to the total stress, the associated back stress vector is divided into its deviatoric and hydrostatic parts, α and $\overline{p}$, respectively:

$$\mathbf{a} = \alpha + \overline{p}\mathbf{i} \quad \text{with} \quad \overline{p} = \frac{\mathrm{tr}(\mathbf{a})}{3} \tag{6}$$

In a deviatoric space the nonlinear kinematic hardening finds the below shape:

$$\dot{\alpha} = \sum_{i=1}^{m} \dot{\alpha}_i, \quad \dot{\alpha}_i = H_{\mathrm{kin},i}\dot{\mathbf{e}}^{\mathrm{p}} - H_{\mathrm{nl},i}\dot{\gamma}\alpha_i \tag{7}$$

where $\mathbf{e}^p$ is created from the strain decomposition. This is the same as the one for the stress:

$$\varepsilon = \mathbf{e} + \frac{\varepsilon_v}{3}\mathbf{i} \quad \text{with} \quad \varepsilon_v = \text{tr}(\varepsilon) \tag{8}$$

In the prior equality, $\mathbf{e}$ stands for the deviatoric strain and ε_v is called volumetric or hydrostatic strain. Elastic and plastic strains stem from these strains as

$$\varepsilon = \varepsilon^e + \varepsilon^p \tag{9}$$

$$\mathbf{e} = \mathbf{e}^e + \mathbf{e}^p \tag{10}$$

$$\varepsilon_v = \varepsilon_v^e + \varepsilon_v^p \tag{11}$$

Using an associative flow rule, the plastic multiplier, $\dot{\gamma}$, holds the connection between the rate of the plastic strain and the yield function gradient as follows:

$$\dot{\varepsilon}^p = \dot{\gamma}\frac{\partial F}{\partial \sigma'} \tag{12}$$

Referring to Eq. (1), the above relation finds the below form:

$$\dot{\varepsilon}^p = \dot{\gamma}\mathbf{s}' + \frac{2}{3}\beta\dot{\gamma}(\tau_y - \beta p')\mathbf{i} \tag{13}$$

Deviatoric and hydrostatic parts of $\dot{\varepsilon}^p$ are easily recognized comparing Eqs. (13) with (8) in the next forms:

$$\dot{\mathbf{e}}^p = \dot{\gamma}\mathbf{s}' \tag{14}$$

$$\dot{\varepsilon}_v^p = 2\beta\dot{\gamma}(\tau_y - \beta p') \tag{15}$$

It is convenient to find τ_y by taking the initial conditions of $\tau_y = \tau_{y,0}$ and $\gamma = 0$ to solve the associated differential equation, Eq. (2), which reaches succeeding equality:

$$\tau_y = \tau_{y,0} + \tau_{y,s}(1 - \exp(-\overline{b}\gamma)) \tag{16}$$

It is crucial to obtain the shifted stress evolution. This goal is fulfilled by Eq. (4) and the generalized Hooke's law reading:

$$\dot{\sigma}' = 2G\dot{\varepsilon}^e + \left(K - \frac{2}{3}G\right)\dot{\varepsilon}_v^e\mathbf{i} - \mathbf{a} \tag{17}$$

Using Eqs. (6)–(8), the rate of the shifted stress finds the following shape:

$$\dot{\sigma}' = 2G\dot{\mathbf{e}}^e - \sum_{i=1}^{m} H_{\text{kin},i}\dot{\mathbf{e}}^p + \sum_{i=1}^{m} H_{\text{nl},i}\dot{\gamma}\alpha_i$$
$$+ \left(K\dot{\varepsilon}_v^e - \sum_{i=1}^{m}\frac{H_{\text{kin},i}}{3}\dot{\varepsilon}_v^p + \sum_{i=1}^{m} H_{\text{nl},i}\dot{\gamma}\frac{\text{tr}(\alpha_i)}{3}\right)\mathbf{i} \tag{18}$$

The preceding equality along with Eqs. (4), (5), (10), (11), (14), and (15) are utilized to achieve the rates of the deviatoric and hydrostatic shifted stresses as

$$\dot{\mathbf{s}}' = 2G\dot{\mathbf{e}} - 2\overline{G}\dot{\gamma}\mathbf{s}' + \sum_{i=1}^{m} H_{\text{nl},i}\dot{\gamma}\alpha_i \tag{19}$$

$$\dot{p}' = K\dot{\varepsilon}_v - 2\beta\dot{\gamma}\overline{K}(\tau_y - \beta p') + \sum_{i=1}^{m} H_{\text{nl},i}\dot{\gamma}\overline{p}_i \tag{20}$$

Where $\overline{K}$ and $\overline{G}$ are constants defined with the subsequent formulae:

$$2\overline{G} = 2G + \sum_{i=1}^{m} H_{\text{kin},i} \tag{21}$$

$$\overline{K} = K + \sum_{i=1}^{m}\frac{H_{\text{kin},i}}{3} \tag{22}$$

As the last measure before computing the plastic multiplier, the rate of the hydrostatic back stress must be attained. This is realized through utilizing Eqs. (3) and (6) having them departed into their deviatoric and volumetric sections and then drawing out $\dot{\overline{p}}$ in the next shape. As guidance, during this mission one needs Eqs. (7) and (8) along with

some manipulations.

$$\dot{\overline{p}} = \sum_{i=1}^{m} \dot{\overline{p}}_i, \quad \dot{\overline{p}}_i = \frac{2}{3}H_{\text{kin},i}\dot{\gamma}\beta(\tau_y - \beta p') - H_{\text{nl},i}\dot{\gamma}\overline{p}_i \tag{23}$$

Consequently, employing the consistency condition, $\dot{F} = 0$ if $F = 0$, during the plastic phase together with Eqs. (1), (2), (19), and (20), the plastic multiplier is computed as

$$\dot{\gamma} = \frac{2G\dot{\mathbf{e}}^T\mathbf{s}' + \sqrt{2}\beta KR\dot{\varepsilon}_v}{2(\overline{G} + \beta^2\overline{K})R^2 + \sqrt{2}R\left[\overline{b}(\tau_{y,0} + \tau_{y,s} - \tau_y) - \beta\sum_{i=1}^{m} H_{\text{nl},i}\overline{p}_i\right] - \mathbf{s}'^T\sum_{i=1}^{m} H_{\text{nl},i}\alpha_i} \tag{24}$$

Where R serves as the yield surface radius having the next relationship:

$$R = \sqrt{2}(\tau_y - \beta p') \tag{25}$$

3. Exponential map integration using two integrating factors, EX

This was first devised by Liu [31] where he integrated the constitutive equations of the elastic-perfectly plastic Drucker–Prager model and then was developed by the authors for the Drucker–Prager plasticity with linear mixed hardening [50]. This section is subject to evolve the scheme to the nonlinear isotropic and kinematic hardenings. The integration algorithm is explained in two major parts; mapping into augmented stress space and stress updating procedure. It is worth mentioning that the formulation is described in detail since many of its parts are needed to be addressed where the new hybrid techniques are developed.

3.1. Mapping into augmented stress space

The heart of exponential based integrations is to map the original constitutive equations into augmented stress space. In this way, the system of nonlinear differential equations is converted to a set of quasi-linear ones. The integrating factor X^0 is defined so that it can satisfy the next two differential equations drawn from Eq. (19):

$$\frac{d}{dt}(X^0\mathbf{s}') = X^0\dot{\mathbf{s}}' + 2\overline{G}\dot{\gamma}X^0\mathbf{s}' \tag{26}$$

$$\frac{d}{dt}(X^0\mathbf{s}') = 2GX^0\dot{\mathbf{e}} + \dot{\gamma}X^0\sum_{i=1}^{m} H_{\text{nl},i}\alpha_i \tag{27}$$

Expanding the first equality and discarding the same parts from both sides contribute to the following differential equation for the integrating factor:

$$\dot{X}^0 = 2\overline{G}\dot{\gamma}X^0 \tag{28}$$

The plastic multiplier from the prior equation is substituted for its counterpart from Eq. (24) which reads

$$\dot{X}^0 = \frac{4G\overline{G}}{Q}\dot{\mathbf{e}}^T\mathbf{s}'X^0 + \frac{2\sqrt{2G}\overline{G}\beta KR}{Q}\dot{\varepsilon}_v X^0 \tag{29}$$

where

$$Q = 2(\overline{G} + \beta^2\overline{K})R^2 + \sqrt{2}R\left[\overline{b}(\tau_{y,0} + \tau_{y,s} - \tau_y) - \beta\sum_{i=1}^{m} H_{\text{nl},i}\overline{p}_i\right]$$
$$-\mathbf{s}'^T\sum_{i=1}^{m} H_{\text{nl},i}\alpha_i \tag{30}$$

After multiplying Eq. (27) by $\mathbf{s}'^T$ and making use of the following relations

$$R^2 = \mathbf{s}'^T\mathbf{s}' \quad \text{and} \quad \dot{R}R = \dot{\mathbf{s}}'^T\mathbf{s}', \tag{31}$$

obtained from the yield function, one can attain the subsequent differential equation:

$$\frac{d}{dt}(X^0 R) = \frac{2G}{R} X^0 \mathbf{s}'^T \dot{\mathbf{e}} + \frac{\dot{\gamma}}{R} X^0 \mathbf{s}'^T \sum_{i=1}^{m} H_{\mathrm{nl},i} \boldsymbol{\alpha}_i \tag{32}$$

The differential equations (27) and (32) comprise the first dynamical system as

$$\dot{\mathbf{X}}_a = \mathbb{A}_a \mathbf{X}_a \tag{33}$$

where $\mathbf{X}_a$ and $\mathbb{A}_a$ are, respectively, called stress vector and control matrix with the coming appearances:

$$\mathbf{X}_a = \left\{ \begin{matrix} \mathbf{X}_a^s \\ X_a^R \end{matrix} \right\} = \left\{ \begin{matrix} X^0 \mathbf{s}' \\ X^0 R \end{matrix} \right\} \quad \text{and}$$

$$\mathbb{A}_a = \begin{bmatrix} \mathbb{O}_{9\times9} & \frac{2G}{R}\dot{\boldsymbol{\mu}} \\ \frac{2G}{R}\dot{\boldsymbol{\mu}}^T & 0 \end{bmatrix}_{10\times10} \quad \text{with} \quad \dot{\boldsymbol{\mu}} = \dot{\mathbf{e}} + \frac{\dot{\gamma}}{2G}\sum_{i=1}^{m} H_{\mathrm{nl},i}\boldsymbol{\alpha}_i \tag{34}$$

Solving this dynamical system, $\mathbf{X}^s$ and X^R are obtained while the integrating factor remains unknown as a key to acquire $\mathbf{s}'$ and R. The more the precise X^0, the more accurate are the updated values. To effectively manage the integrating factor with as much accuracy, another dynamical system is introduced as

$$\dot{\mathbf{X}}_b = \mathbb{A}_b \mathbf{X}_b \tag{35}$$

which includes a new integrating factor denoted by x^0. The basic concept to draw this system is the function of the yield surface radius containing two significant variables of τ_y and p'. Differentiating both sides of Eq. (25) with respect to pseudo-time alongside utilizing Eqs. (2) and (20) result in

$$\dot{R} = \sqrt{2}\left(\overline{b}(\tau_{y,0} + \tau_{y,s} - \tau_y)\dot{\gamma} - \beta(K\dot{\varepsilon}_v - 2\beta\dot{\gamma}\overline{K}(\tau_y - \beta p') + \sum_{i=1}^{m} H_{\mathrm{nl},i}\dot{\gamma}\overline{p}_i) \right) \tag{36}$$

Using Eq. (24) to substitute for the plastic multiplier and after lots of manipulations, the previous relationship is transformed into the next desired form:

$$\dot{R} = 2\sqrt{2}\overline{K}\beta^2\dot{\gamma}(\tau_y - \beta p') + 2G\overline{Q}\dot{\mathbf{e}}^T\mathbf{s}' + \sqrt{2}\left(\overline{Q} - \frac{1}{R}\right)\beta K\dot{\varepsilon}_v \tag{37}$$

with

$$\overline{Q} = \frac{\sqrt{2}}{Q}\left[\overline{b}(\tau_{y,0} + \tau_{y,s} - \tau_y) - \beta \sum_{i=1}^{m} H_{\mathrm{nl},i}\overline{p}_i \right] \tag{38}$$

At this time, the new integrating factor is coined so it could fulfill the following equality:

$$\frac{d}{dt}\left[x^0(\tau_y - \beta p') \right] = \left[\left(\overline{Q} - \frac{1}{R}\right)\beta K\dot{\varepsilon}_v + \sqrt{2}\overline{Q}G\dot{\mathbf{e}}^T\mathbf{s}' \right]x^0 \tag{39}$$

Working on the previous relationship, one can reach the below form:

$$\frac{d}{dt}(\tau_y - \beta p') = \left(\overline{Q} - \frac{1}{R}\right)\beta K\dot{\varepsilon}_v + \sqrt{2}\overline{Q}G\dot{\mathbf{e}}^T\mathbf{s}' - \frac{\dot{x}^0}{x^0}(\tau_y - \beta p') \tag{40}$$

Comparing both sides of Eqs. (37) and (40), the coming differential equation is managed for the new integrating factor:

$$\dot{x}^0 = -2\overline{K}\beta^2\dot{\gamma}x^0 \tag{41}$$

The next form is conveniently attained by manipulating Eq. (39) along with taking its derivative with respect to $(\tau_y - \beta p')$:

$$\frac{d}{dt}(x^0 R) = \frac{2}{R}\left[\left(\overline{Q} - \frac{1}{R}\right)\beta K\dot{\varepsilon}_v + \sqrt{2}\overline{Q}G\dot{\mathbf{e}}^T\mathbf{s}' \right](\tau_y - \beta p')x^0 \tag{42}$$

Utilizing Eq. (42) alongside the following appearance of Eq. (39)

$$\frac{d}{dt}\left[x^0(\tau_y - \beta p') \right] = \frac{1}{R}\left[\left(\overline{Q} - \frac{1}{R}\right)\beta K\dot{\varepsilon}_v + \sqrt{2}\overline{Q}G\dot{\mathbf{e}}^T\mathbf{s}' \right]Rx^0, \tag{43}$$

yields the next system of differential equations as

$$\frac{d}{dt}\left\{ \begin{matrix} x^0 R \\ x^0(\tau_y - \beta p') \end{matrix} \right\} = \frac{1}{R}\left[\left(\overline{Q} - \frac{1}{R}\right)\beta K\dot{\varepsilon}_v + \sqrt{2}\overline{Q}G\dot{\mathbf{e}}^T\mathbf{s}' \right] \left\{ \begin{matrix} 2x^0(\tau_y - \beta p') \\ x^0 R \end{matrix} \right\} \tag{44}$$

This could be reshaped in term of the dynamical system (35) as

$$\mathbb{A}_b = \frac{1}{R}\left[\left(\overline{Q} - \frac{1}{R}\right)\beta K\dot{\varepsilon}_v + \sqrt{2}\overline{Q}G\dot{\mathbf{e}}^T\mathbf{s}' \right] \begin{bmatrix} 0 & 2 \\ 1 & 0 \end{bmatrix} \quad \text{and}$$

$$\mathbf{X}_b = \left\{ \begin{matrix} X_b^R \\ X_b^1 \end{matrix} \right\} = \left\{ \begin{matrix} x^0 R \\ x^0(\tau_y - \beta p') \end{matrix} \right\} \tag{45}$$

Having used the initial conditions to solve the differential equations (28) and (41) as

$$X^0 = \exp(2\overline{G}\gamma) \quad \text{and} \quad x^0 = \exp(-2\overline{K}\beta^2\gamma), \tag{46}$$

one can acquire the connection between the two integrating factors as follows:

$$x^0 = (X^0)^{-\overline{K}\beta^2/\overline{G}} \tag{47}$$

Considering the control matrixes $\mathbb{A}_a$ and $\mathbb{A}_b$ as the matrixes with their elements independent of time, the two dynamical systems Eq. (33) and (35) are converted into two sets of linear differentials having the following closed solutions:

$$\mathbf{X}_a(t) = \exp(\mathbb{A}_a t)\mathbf{X}_a(0); \quad \mathbf{X}_a(0) = \left\{ \begin{matrix} \mathbf{X}_{a,0}^s \\ X_{a,0}^R \end{matrix} \right\} = \left\{ \begin{matrix} \mathbf{s}'_0 \\ \sqrt{2}(\tau_{y,0} - \beta p'_0) \end{matrix} \right\} \tag{48}$$

$$\mathbf{X}_b(t) = \exp(\mathbb{A}_b t)\mathbf{X}_b(0); \quad \mathbf{X}_b(0) = \left\{ \begin{matrix} X_{b,0}^1 \\ X_{b,0}^0 \end{matrix} \right\} = (\tau_{y,0} - \beta p'_0)\left\{ \begin{matrix} \sqrt{2} \\ 1 \end{matrix} \right\} \tag{49}$$

3.2. Stress updating procedure

To obtain the numerical algorithm, a rectilinear strain-controlled path is assumed, where $\dot{\mathbf{e}}$ and $\dot{\varepsilon}_v$ are unvarying within each incremental pace. It is also assumed that the stress state at time $t = t_n$ is on the yield surface, i.e. $F = (1/2)\mathbf{s}'_n{}^T\mathbf{s}'_n - (\tau_{y,n} - \beta p'_n)^2 = 0$. Following an explicit scheme, the yield surface radius is reckoned with its amount at the outset of each time step. Thus, the control matrixes $\mathbb{A}_a$ and $\mathbb{A}_b$ are independent of augmented stress vectors $\mathbf{X}_a$ and $\mathbf{X}_b$, consequently, the desired numerical algorithm reaches the following shapes:

$$\mathbf{X}_{a,n+1} = \exp(\mathbb{A}_{a,n}\Delta t)\mathbf{X}_{a,n} = \mathbb{G}_{a,n}\mathbf{X}_{a,n} \tag{50}$$

$$\mathbf{X}_{b,n+1} = \exp(\mathbb{A}_{b,n}\Delta t)\mathbf{X}_{b,n} = \mathbb{G}_{b,n}\mathbf{X}_{b,n} \tag{51}$$

where the matrix exponentials, $\mathbb{G}_{a,n}$ and $\mathbb{G}_{b,n}$, are computed as

$$\mathbb{G}_{a,n} = \begin{bmatrix} \mathbb{I}_{9\times9} + (a_n - 1)\Delta\hat{\boldsymbol{\mu}}\Delta\hat{\boldsymbol{\mu}}^T & b_n\Delta\hat{\boldsymbol{\mu}} \\ b_n\Delta\hat{\boldsymbol{\mu}}^T & a_n \end{bmatrix}_{10\times10} \quad \text{and}$$

$$\mathbb{G}_{b,n} = \begin{bmatrix} u_n & \sqrt{2}v_n \\ \frac{1}{\sqrt{2}}v_n & u_n \end{bmatrix} \tag{52}$$

with

$$\Delta\hat{\boldsymbol{\mu}} = \frac{\Delta\boldsymbol{\mu}}{\|\Delta\boldsymbol{\mu}\|} \quad \text{with} \quad \Delta\boldsymbol{\mu} = \Delta\mathbf{e} + \frac{\lambda}{2G}\sum_{i=1}^{m} H_{\mathrm{nl},i}\boldsymbol{\alpha}_{n,i} \tag{53}$$

$$a_n = \cosh\left(\frac{2G}{R_n}\|\Delta\boldsymbol{\mu}\|\right) \quad \text{and} \quad b_n = \sinh\left(\frac{2G}{R_n}\|\Delta\boldsymbol{\mu}\|\right) \tag{54}$$

$$u_n = \cosh\left(\frac{1}{R_n}\left[\left(\overline{Q}_n - \frac{1}{R_n}\right)\beta K\Delta\varepsilon_v + \sqrt{2}\overline{Q}_n G\Delta\mathbf{e}^T\mathbf{s}'_n \right]\right) \tag{55}$$

$$v_n = \sinh\left(\frac{1}{R_n}\left[\left(\overline{Q}_n - \frac{1}{R_n}\right)\beta K\Delta\varepsilon_v + \sqrt{2}\overline{Q}_n G\Delta\mathbf{e}^T\mathbf{s}'_n\right]\right) \tag{56}$$

In these relationships, the parameter λ represents the discrete plastic multiplier calculated through

$$\lambda = \dot{\gamma}\Delta t$$

$$= \frac{2G\Delta\mathbf{e}^T\mathbf{s}'_n + \sqrt{2}\beta K R_n\Delta\varepsilon_v}{2(\overline{G}+\beta^2\overline{K})R_n^2 + \sqrt{2}R_n\left[\overline{b}(\tau_{y,0}+\tau_{y,s}-\tau_{y,n})-\beta\sum\limits_{i=1}^{m}H_{\mathrm{nl},i}\overline{p}_{i,n}\right] - \mathbf{s}'_n{}^T\sum\limits_{i=1}^{m}H_{\mathrm{nl},i}\boldsymbol{\alpha}_{i,n}} \tag{57}$$

The stress vectors $\mathbf{X}_a$ and $\mathbf{X}_b$ are updated by means of Eqs. (50) and (51). Having X_a^R and X_b^R from the updated stress vectors and utilizing Eq. (47), one can gain the integrating factor X^0 with the below appearance:

$$X_{n+1}^0 = \left(\frac{X_{a,n+1}^R}{X_{b,n+1}^R}\right)^{\overline{G}/(\overline{K}\beta^2+\overline{G})} \tag{58}$$

Subsequently, the deviatoric shifted stress and the yield surface radius are computed through

$$\mathbf{s}'_{n+1} = \frac{\mathbf{X}_{n+1}^s}{X_{n+1}^0} \quad \text{and} \quad R_{n+1} = \frac{X_{n+1}^R}{X_{n+1}^0} \tag{59}$$

As the below relationship suggests, the back stress must be updated in order to sort out the deviatoric stress, $\mathbf{s}$, at the end of each load step:

$$\mathbf{s}'_{n+1} = \mathbf{s}_{n+1} - \boldsymbol{\alpha}_{n+1} \quad \text{with} \quad \mathbf{s}_{n+1} = \mathbf{s}_n + 2G(\Delta\mathbf{e}-\Delta\mathbf{e}^p) \tag{60}$$

With the purpose of updating the back stress vector, the differential equation (7) is integrated to have the next incremental shape:

$$\boldsymbol{\alpha}_{n+1} - \boldsymbol{\alpha}_n = \sum_{i=1}^{m}\int_{t_n}^{t_{n+1}}(H_{\mathrm{kin},i}\dot{\mathbf{e}}^p - H_{\mathrm{nl},i}\dot{\gamma}\boldsymbol{\alpha}_i)dt \tag{61}$$

To work out the previous integration, $\boldsymbol{\alpha}_i$ needs to be assumed constant. It is of better accuracy to estimate the $\boldsymbol{\alpha}_i$ by its value at the middle of each time step, which means

$$\boldsymbol{\alpha}_i = \frac{\boldsymbol{\alpha}_{n+1,i}+\boldsymbol{\alpha}_{n,i}}{2} \tag{62}$$

Having the prior equality replaced for $\boldsymbol{\alpha}_i$ in Eq. (61) leads to the below relationship for the back stress:

$$\boldsymbol{\alpha}_{n+1} = \sum_{i=1}^{m}\left(\frac{2-\overline{\lambda}H_{\mathrm{nl},i}}{2+\overline{\lambda}H_{\mathrm{nl},i}}\boldsymbol{\alpha}_{n,i} + \frac{2H_{\mathrm{kin},i}}{2+\overline{\lambda}H_{\mathrm{nl},i}}\Delta\mathbf{e}^p\right) \tag{63}$$

The evolution of the deviatoric plastic strain is readily acquired using the preceding equality along with Eq. (60) as

$$\Delta\mathbf{e}^p = \frac{1}{2G+\sum\limits_{i=1}^{m}\frac{2H_{\mathrm{kin},i}}{2+\overline{\lambda}H_{\mathrm{nl},i}}}\left(\mathbf{s}_n + 2G\Delta\mathbf{e} - \mathbf{s}'_{n+1} - \sum_{i=1}^{m}\frac{2-\overline{\lambda}H_{\mathrm{nl},i}}{2+\overline{\lambda}H_{\mathrm{nl},i}}\boldsymbol{\alpha}_{n,i}\right) \tag{64}$$

In this relationship, the discrete plastic multiplier should be computed through the following, which is obtained by solving Eq. (28) considering the initial condition of $X^0(\gamma=0)=1$ as

$$\overline{\lambda} = \frac{1}{2\overline{G}}\ln\left(\frac{X_{n+1}^0}{X_n^0}\right) \tag{65}$$

Up until now, the parameters $\mathbf{s}'_{n+1}$, $\mathbf{s}_{n+1}$, $\boldsymbol{\alpha}_{n+1}$, and R_{n+1} have been attained. The only variables to update are p', $\overline{p}$ and τ_y. The coming equality, which is conceived through Eq. (14) and the yield surface function, helps obtain the variables via using the well computed $\Delta\mathbf{e}^p$ for having better accuracy:

$$\|\dot{\mathbf{e}}^p\| = \dot{\gamma}\|\mathbf{s}'\| = \dot{\gamma}R \tag{66}$$

Using the prior equation alongside the constitutive equation (20), the hydrostatic shifted stress is updated as

$$p'_{n+1} = p'_n + K\Delta\varepsilon_v - \sqrt{2}\beta\overline{K}\|\Delta\mathbf{e}^p\| + \overline{\lambda}\sum_{i=1}^{m}H_{\mathrm{nl},i}\overline{p}_{n,i} \tag{67}$$

Referring to Eq. (25), computing p'_{n+1} and R_{n+1} means having $\tau_{y,n+1}$ with the following appearance:

$$\tau_{y,n+1} = \frac{R_{n+1}}{\sqrt{2}} + \beta p'_{n+1} \tag{68}$$

The same procedure, as was performed for $\boldsymbol{\alpha}$ and p', is utilized to update the volumetric part of the back stress. In the constitutive equation (23), the estimation $\overline{p}_i = (\overline{p}_{n,i}+\overline{p}_{n+1,i})/2$ and Eq. (66) are exploited to reach the coming form:

$$\overline{p}_{n+1} = \sum_{i=1}^{m}\frac{1}{2+\overline{\lambda}H_{\mathrm{nl},i}}\left[(2-\overline{\lambda}H_{\mathrm{nl},i})\overline{p}_{n,i} + \frac{2\sqrt{2}}{3}H_{\mathrm{kin},i}\beta\|\Delta\mathbf{e}^p\|\right] \tag{69}$$

4. Hybrid exponential map-forward Euler integration, HXF

A growing number of variables need to be updated as the plasticity models become more advanced. Following an explicit manner, the problem is dealt with through assuming more variables as constants with their amounts at beginning of each time-step during the increments of the integration process. However, this would aggravate the outcomes of the explicit methods such as Forward Euler and Exponential map. On the other side, it is not wise to forsake explicit integrations and their advantages such as easy implementation and speed. This will encourage developing a new explicit algorithm based on the two well-known explicit schemes of Exponential Map and Forward Euler.

Overall, the Exponential Map integrations are more accurate and efficient than the Forward Euler's except for the fact that the latter is faster than the former, see [36,37,50]. Consequently, the hybrid scheme would better form based on the Exponential map with some helps from the Froward Euler algorithm. In the proposed scheme, the Forward Euler algorithm is firstly used to update the variables at the middle of each load step, and then the computed values are substituted for the amounts which used to be approximated constant in a regular exponential scheme. This will significantly improve the results and increase the rate of convergence.

Therefore, the variables are updated via a two-step procedure; computing the values at the middle of the load increment through a Forward Euler scheme and then, utilizing the results of the previous step to update the parameters with the Exponential map scheme. The following elaborate the algorithm.

4.1. Forward Euler step

The discrete plastic multiplier is calculated for the half of the load increment:

$$\lambda' = \frac{1}{2}\dot{\gamma}\Delta t \tag{70}$$

where $\dot{\gamma}$ will be replaced with Eq. (24). Having the discrete plastic multiplier and using the constitutive equations (16), (19), (20), (23), (14), and (7), all the variables are updated at the middle of each load step as

$$\mathbf{s}'^m = \mathbf{s}'_{(n+1)/2} = \mathbf{s}'_n + G\Delta\mathbf{e} - 2\overline{G}\lambda'\mathbf{s}'_n + \lambda'\sum_{i=1}^{m}H_{\mathrm{nl},i}\boldsymbol{\alpha}_{n,i} \tag{71}$$

$$p'^m = p'_{(n+1)/2} = p'_n + \frac{1}{2}K\Delta\varepsilon_v - 2\beta\lambda'\overline{K}(\tau_{y,n}-\beta p'_n) + \sum_{i=1}^{m}H_{\mathrm{nl},i}\lambda'\overline{p}_n \tag{72}$$

$$\tau_y^m = \tau_{y,(n+1)/2} = \tau_{y,0} + \tau_{y,s}(1 - \exp(-\bar{b}\gamma^m)) \quad \text{with} \quad \gamma^m = \gamma_n + \lambda' \tag{73}$$

$$\begin{aligned}\bar{p}^m = \bar{p}_{(n+1)/2} &= \sum_{i=1}^{m} \bar{p}_i^m \\ &= \sum_{i=1}^{m}\left(\bar{p}_{n,i} + \frac{2}{3}H_{\text{kin},i}\lambda'\beta(\tau_{y,n} - \beta p'_n) - \lambda' H_{\text{nl},i}\bar{p}_{n,i}\right)\end{aligned} \tag{74}$$

$$\alpha^m = \alpha_{(n+1)/2} = \sum_{i=1}^{m}\alpha_i^m = \sum_{i=1}^{m}(\alpha_{n,i} + \lambda'(H_{\text{kin},i}\mathbf{s}'_n - H_{\text{nl},i}\alpha_{n,i})) \tag{75}$$

The yield surface radius is obtained using Eqs. (72) and (73):

$$R^m = R_{(n+1)/2} = \sqrt{2}(\tau_y^m - \beta p'^m) \tag{76}$$

To fulfill the consistency condition, the deviatoric shifted stress must be rectified adding the correcting vector normal to the yield surface through the next process:

$$\mathbf{s}'^m = \mathbf{s}'^m + a_f \mathbf{n}^m \tag{77}$$

with

$$\mathbf{n}^m = \frac{\mathbf{s}'^m}{\|\mathbf{s}'^m\|} \quad \text{and} \quad a_f = \sqrt{((\mathbf{n}^m)^{\text{T}}\mathbf{s}'^m)^2 - \|\mathbf{s}'^m\|^2 + (R^m)^2} - (\mathbf{n}^m)^{\text{T}}\mathbf{s}'^m. \tag{78}$$

4.2. Exponential map step

At this step the whole load increment is performed again, and the integration is carried out following an Exponential Map scheme along with the results of the previous step. The discrete plastic multiplier is computed by the way of Eq. (24) and the equalities (71)–(77) as

$$\lambda^m = \frac{2G\Delta\mathbf{e}^{\text{T}}\mathbf{s}'^m + \sqrt{2}\beta KR^m\Delta\varepsilon_v}{2(\bar{G}+\beta^2\bar{K})(R^m)^2 + \sqrt{2}R^m\left[\bar{b}(\tau_{y,0}+\tau_{y,s}-\tau_y^m) - \beta\sum\limits_{i=1}^{m}H_{\text{nl},i}\bar{p}_i^m\right] - (\mathbf{s}'^m)^{\text{T}}\sum\limits_{i=1}^{m}H_{\text{nl},i}\alpha_i^m} \tag{79}$$

The dynamical systems (50) and (51) are adapted to these forms:

$$\mathbf{X}_{a,n+1} = \exp(\mathbb{A}_a^m\Delta t)\mathbf{X}_{a,n} = \mathbb{G}_a^m\mathbf{X}_{a,n} \tag{80}$$

$$\mathbf{X}_{b,n+1} = \exp(\mathbb{A}_b^m\Delta t)\mathbf{X}_{b,n} = \mathbb{G}_b^m\mathbf{X}_{b,n} \tag{81}$$

where the matrix exponentials $\mathbb{G}_a^m$ and $\mathbb{G}_b^m$ are computed through

$$\mathbb{G}_a^m = \begin{bmatrix} \mathbb{I}_{9\times9} + (a^m-1)\Delta\boldsymbol{\mu}^m(\Delta\hat{\boldsymbol{\mu}}^m)^{\text{T}} & b^m\Delta\hat{\boldsymbol{\mu}}^m \\ b^m\Delta\hat{\boldsymbol{\mu}}^{m\text{T}} & a^m \end{bmatrix}_{10\times10} \quad \text{and}$$

$$\mathbb{G}_b^m = \begin{bmatrix} u^m & \sqrt{2}v^m \\ \frac{1}{\sqrt{2}}v^m & u^m \end{bmatrix} \tag{82}$$

with

$$\Delta\hat{\boldsymbol{\mu}}^m = \frac{\Delta\boldsymbol{\mu}^m}{\|\Delta\boldsymbol{\mu}^m\|} \quad \text{with} \quad \Delta\boldsymbol{\mu}^m = \Delta\mathbf{e} + \frac{\lambda}{2G}\sum_{i=1}^{m}H_{\text{nl},i}\alpha^m \tag{83}$$

$$a^m = \cosh\left(\frac{2G}{R^m}\|\Delta\boldsymbol{\mu}^m\|\right) \quad \text{and} \quad b^m = \sinh\left(\frac{2G}{R^m}\|\Delta\boldsymbol{\mu}^m\|\right) \tag{84}$$

$$u^m = \cosh\left(\frac{1}{R^m}\left[\left(\bar{Q}^m - \frac{1}{R^m}\right)\beta K\Delta\varepsilon_v + \sqrt{2}\bar{Q}^m G\Delta\mathbf{e}^{\text{T}}\mathbf{s}'^m\right]\right) \tag{85}$$

$$v^m = \sinh\left(\frac{1}{R^m}\left[\left(\bar{Q}^m - \frac{1}{R^m}\right)\beta K\Delta\varepsilon_v + \sqrt{2}\bar{Q}^m G\Delta\mathbf{e}^{\text{T}}\mathbf{s}'^m\right]\right) \tag{86}$$

$$\bar{Q}^m = \frac{\sqrt{2}}{Q^m}\left[\bar{b}(\tau_{y,0}+\tau_{y,s}-\tau_y^m) - \beta\sum_{i=1}^{m}H_{\text{nl},i}\bar{p}_i^m\right] \tag{87}$$

$$Q^m = 2(\bar{G}+\beta^2\bar{K})(R^m)^2 + \sqrt{2}R^m\left[\bar{b}(\tau_{y,0}+\tau_{y,s}-\tau_y^m) - \beta\sum_{i=1}^{m}H_{\text{nl},i}\bar{p}_i^m\right]$$
$$- (\mathbf{s}'^m)^{\text{T}}\sum_{i=1}^{m}H_{\text{nl},i}\alpha_i^m \tag{88}$$

Solving the two dynamical systems (80) and (81), and also securing the integrating factor from Eq. (58), the deviatoric shifted stress and the yield surface radius are computed by Eq. (59). The deviatoric part of the back stress vector is updated through equalities (60) and (61) except that α_i^m ought to be substituted for α_i resulting in

$$\alpha_{n+1} = \sum_{i=1}^{m}(\alpha_{n,i} + H_{\text{kin},i}\Delta\mathbf{e}^{\text{p}} - H_{\text{nl},i}\bar{\lambda}\alpha_i^m) \tag{89}$$

$$\Delta\mathbf{e}^{\text{p}} = \frac{1}{2G}\left(\mathbf{s}_n + 2G\Delta\mathbf{e} - \mathbf{s}'_{n+1} - \sum_{i=1}^{m}(\alpha_{n,i} - H_{\text{nl},i}\bar{\lambda}\alpha_i^m)\right) \tag{90}$$

Where $\bar{\lambda}$ is computed from Eq. (65). To update the volumetric shifted and back stresses, p' and $\bar{p}$, the constitutive equations (20) and (23) are utilized alongside τ_y^m, p'^m, and $\bar{p}^m$ from Eqs. (72)–(74) that reach the following relationships:

$$p'_{n+1} = p'_n + K\Delta\varepsilon_v - 2\beta\bar{\lambda}\bar{K}(\tau_y^m - \beta p'^m) + \sum_{i=1}^{m}H_{\text{nl},i}\bar{\lambda}\bar{p}^m \tag{91}$$

$$\bar{p}_{n+1} = \sum_{i=1}^{m}\bar{p}_{n+1,i} = \sum_{i=1}^{m}\left(\bar{p}_{n,i} + \frac{2}{3}H_{\text{kin},i}\bar{\lambda}\beta(\tau_y^m - \beta p'^m) - \bar{\lambda}H_{\text{nl},i}\bar{p}_i^m\right) \tag{92}$$

Having managed to acquire R_{n+1} and p'_{n+1}, one can easily obtain the shear stress from Eq. (68).

5. Semi-implicit exponential map integration, EXS

Rezaiee Pajand and Nasirai [35] first developed this scheme for the elastic perfectly plastic Drucker–Prager model. They improved the newly introduced Exponential Map integration at that time into a second-order algorithm with better accuracy. In this section, the algorithm is progressed to take account of the nonlinear isotropic and kinematic hardenings. The purpose is to achieve a second-order integration so it could be compared with the proposed scheme, HXF, in numerical tests. Since the relationships are mainly based on the formulations derived in the exponential map division, Section 3, a summary of the algorithm is presented focusing on the tricky parts.

The algorithm is performed in two general steps. First, the parameters are updated at the middle of each load step and then the entire process is carried out again using the obtained amounts from the preceding step to be substituted for the variables that used to be presumed constant in an ordinary exponential scheme. The discrete plastic multiplier is the same as λ' from Eq. (70) to build the coming dynamical systems of

$$\mathbf{X}_{a,(n+1)/2} = \exp(\mathbb{A}'_{a,n}\Delta t)\mathbf{X}_{a,n} = \mathbb{G}'_{a,n}\mathbf{X}_{a,n} \tag{93}$$

$$\mathbf{X}_{b,(n+1)/2} = \exp(\mathbb{A}'_{b,n}\Delta t)\mathbf{X}_{b,n} = \mathbb{G}'_{b,n}\mathbf{X}_{b,n} \tag{94}$$

where the matrix exponentials, $\mathbb{G}'_{a,n}$ and $\mathbb{G}'_{b,n}$, are computed via Eq. (52) except that $\Delta\boldsymbol{\mu}$, $\Delta\hat{\boldsymbol{\mu}}$, a_n, b_n, u_n and v_n should be replaced for

$$\Delta\hat{\boldsymbol{\mu}}' = \frac{\Delta\boldsymbol{\mu}'}{\|\Delta\boldsymbol{\mu}'\|} \quad \text{with} \quad \Delta\boldsymbol{\mu}' = \frac{\Delta\mathbf{e}}{2} + \frac{\lambda'}{2G}\sum_{i=1}^{m}H_{\text{nl},i}\alpha_{n,i} \tag{95}$$

$$a'_{b,(n+1)/2} = \cosh\left(\frac{2G}{R_n}\|\Delta\boldsymbol{\mu}'\|\right) \quad \text{and} \quad b'_{b,(n+1)/2} = \sinh\left(\frac{2G}{R_n}\|\Delta\boldsymbol{\mu}'\|\right) \tag{96}$$

$$u_{b,(n+1)/2} = \cosh\left(\frac{1}{R_n}\left[\frac{1}{2}\left(\overline{Q}_n - \frac{1}{R_n}\right)\beta K \Delta\varepsilon_v + \frac{\sqrt{2}}{2}\overline{Q}_n G \Delta \mathbf{e}^{\mathrm{T}}\mathbf{s}'_n\right]\right) \quad (97)$$

$$v_{b,(n+1)/2} = \sinh\left(\frac{1}{R_n}\left[\frac{1}{2}\left(\overline{Q}_n - \frac{1}{R_n}\right)\beta K \Delta\varepsilon_v + \frac{\sqrt{2}}{2}\overline{Q}_n G \Delta \mathbf{e}^{\mathrm{T}}\mathbf{s}'_n\right]\right) \quad (98)$$

Having solved the two dynamical systems of Eqs. (93) and (94), one can acquire the integrating factor as

$$X^0_{(n+1)/2} = \left(\frac{X^{\mathrm{R}}_{a,(n+1)/2}}{X^{\mathrm{R}}_{b,(n+1)/2}}\right)^{\overline{G}/(\overline{K}\beta^2 + \overline{G})}, \quad (99)$$

from which the components of the shifted stress and the yield surface radius read,

$$\mathbf{s}'_{(n+1)/2} = \frac{\mathbf{X}^{\mathrm{s}}_{(n+1)/2}}{X^0_{(n+1)/2}} \quad (100)$$

$$p'_{(n+1)/2} = p'_n + \frac{1}{2}K\Delta\varepsilon_v - 2\beta\overline{\lambda K}(\tau_{y,n} - \beta p'_n) + \sum_{i=1}^{m} H_{\mathrm{nl},i}\overline{\lambda}\overline{p}_{n,i} \quad (101)$$

$$R_{(n+1)/2} = \frac{X^{\mathrm{R}}_{(n+1)/2}}{X^0_{(n+1)/2}} \quad (102)$$

with the discrete plastic multiplier of

$$\overline{\lambda} = \frac{1}{2\overline{G}}\ln\left(\frac{X^0_{(n+1)/2}}{X^0_n}\right). \quad (103)$$

By obtaining p' and R from Eqs. (101) and (102), the shear stress has inevitably been managed as

$$\tau_{y,(n+1)/2} = \frac{R_{(n+1)/2}}{\sqrt{2}} + \beta p'_{(n+1)/2} \quad (104)$$

As the back stress vector is computed via the succeeding equalities, the step 1 is concluded.

$$\boldsymbol{\alpha}_{(n+1)/2} = \sum_{i=1}^{m}\boldsymbol{\alpha}_i^{\mathrm{m}} = \sum_{i=1}^{m}(\boldsymbol{\alpha}_{n,i} + \lambda'(H_{\mathrm{kin},i}\mathbf{s}'_n - H_{\mathrm{nl},i}\boldsymbol{\alpha}_{n,i})) \quad (105)$$

$$\overline{p}_{(n+1)/2} = \sum_{i=1}^{m}\overline{p}_i^{\mathrm{m}} = \sum_{i=1}^{m}\left(\overline{p}_{n,i} + \frac{2}{3}H_{\mathrm{kin},i}\lambda'\beta(\tau_{y,n} - \beta p'_n) - \lambda' H_{\mathrm{nl},i}\overline{p}_{n,i}\right) \quad (106)$$

The second step of the scheme is the same as the exponential step of the preceding Hybrid technique, which was thoroughly explained, and therefore, it does not need recurring again.

6. Hybrid exponential map-backward Euler integration, HXB

This scheme is formed of the exponential and Backward Euler integrations to gather their benefits and clearing away their drawbacks. Examining the constituent algorithms reveals that the Backward Euler integration is more capable than the Exponential map when computing the magnitude of the stress while the Exponential integration performs much better at finding the stress's direction [50]. Since the integrations are each competent in a different area, the upside of each one is the downside of another, merging them with each other could potentially lead to a much more powerful scheme.

Regarding the fundamental essence of each strategy, the proposed integration, HXB, is best reached where the direction of the stress is updated by the exponential algorithm and the magnitude through the Backward Euler scheme. Hence, the two schemes are only partially required. Clearly, the direction of the total stress is determined by the direction of the deviatoric shifted stress and the back stress and as a result they should be computed through Exponential algorithm. Given that the total stress

magnitude is contributed by p', $\overline{p}$, and the magnitude of $\mathbf{s}$, it needs to be obtained utilizing the Backward Euler technique. Of course, this was a general description of the Hybrid Scheme and there are, for sure, more intricacies which would better to elaborate during the algorithm debut as follows. Hence, the Hybrid scheme comprises two phases of Exponential Map and Backward Euler.

6.1. Exponential phase

The stresses, $\mathbf{s}'_n$ and p'_n, alongside the yield surface radius, R_n, are utilized to compute the explicit discrete plastic multiplier Eq. (57) denoted by λ^{ex}. This will provide the solution of the dynamical system Eq. (50) through Eqs. (52)–(54) which results in $\mathbf{X}^{\mathrm{s}}_{n+1}$ and $\mathbf{X}^{\mathrm{R}}_{n+1}$. The deviatoric part of the back stress is updated by the means of Eqs. (63)–(65). Note that, in this strategy, there is no need for the second dynamical system, Eq. (51), and its pertinent computations. Thus, having reckoned the stress vector and the updated deviatoric back stress, it is time to enter the Backward Euler Phase concluding the integration scheme.

6.2. Backward Euler phase

The first step, which is also the most time-consuming part of the algorithm, is evaluating the implicit discrete plastic multiplier, λ^{im}. This will demand solving the complex nonlinear Eq. (A.10) carried out by the Newton–Raphson method as if explained in Appendix A. Though, here, there is the momentous asset of exploiting the already-obtained explicit plastic multiplier which can be used as an initial solution for the repetitive Newton–Raphson procedure. This will dramatically drop the number of iterations and boost the analyzing time up to 45% as a compensation for the time added to the regular Backward Euler integration by the Exponential Phase. The recompense is so good that it even makes the whole integration scheme faster than Backward Euler as much as 15%. Securing the implicit discrete plastic multiplier, one can readily update $\tau_{y,n+1}$, p'_{n+1}, and $\overline{p}_{n+1}$ through equalities (A.7)–(A.9). The yield surface radius is obtained via Eq. (25). At this time, the integrating factor X^0_{n+1} is computed as

$$X^0_{n+1} = \frac{X^{\mathrm{R}}_{n+1}}{R_{n+1}} \quad (107)$$

The updated stress vectors from the Exponential Phase together with X^0_{n+1} are employed to obtain the deviatoric shifted stress with the following appearance:

$$\mathbf{s}'^{\mathrm{ex}}_{n+1} = \frac{\mathbf{X}^{\mathrm{s}}_{n+1}}{X^0_{n+1}} \quad (108)$$

In this equality, $\mathbf{s}'^{\mathrm{ex}}_{n+1}$ presents the updated deviatoric shifted stress through Exponential Map, which was truly superscript. As a matter of fact, the magnitude of this vector is not as accurate as its direction so it needs modifying. Actually, the final deviatoric shifted stress would be a vector with the same direction as $\mathbf{s}'^{\mathrm{ex}}_{n+1}$ but the magnitude of $\mathbf{s}'^{\mathrm{back}}_{n+1}$, its Backward Euler counterpart attained by Eq. (A.6) in Appendix A. The following equalities feature the procedure:

$$\|\mathbf{s}'_{n+1}\| = \|\mathbf{s}'^{\mathrm{back}}_{n+1}\| = \sqrt{2}(\tau_{y,n+1} - \beta p'_{n+1}) = R_{n+1} \quad (109)$$

$$\mathbf{s}'_{n+1} = \mathbf{s}'^{\mathrm{ex}}_{n+1} + a\mathbf{n}^{\mathrm{ex}}_{n+1} \quad (110)$$

$$a = \sqrt{((\mathbf{n}^{\mathrm{ex}}_{n+1})^{\mathrm{T}}\mathbf{s}'^{\mathrm{ex}}_{n+1})^2 - \|\mathbf{s}'^{\mathrm{ex}}_{n+1}\|^2 + 2(\tau_{y,n+1} - \beta p'_{n+1})^2} - (\mathbf{n}^{\mathrm{ex}}_{n+1})^{\mathrm{T}}\mathbf{s}'^{\mathrm{ex}}_{n+1} \quad (111)$$

To more conceivably present the new scheme, a flow chart is provided in Fig. 1, which depicts an overview of the whole algorithm.
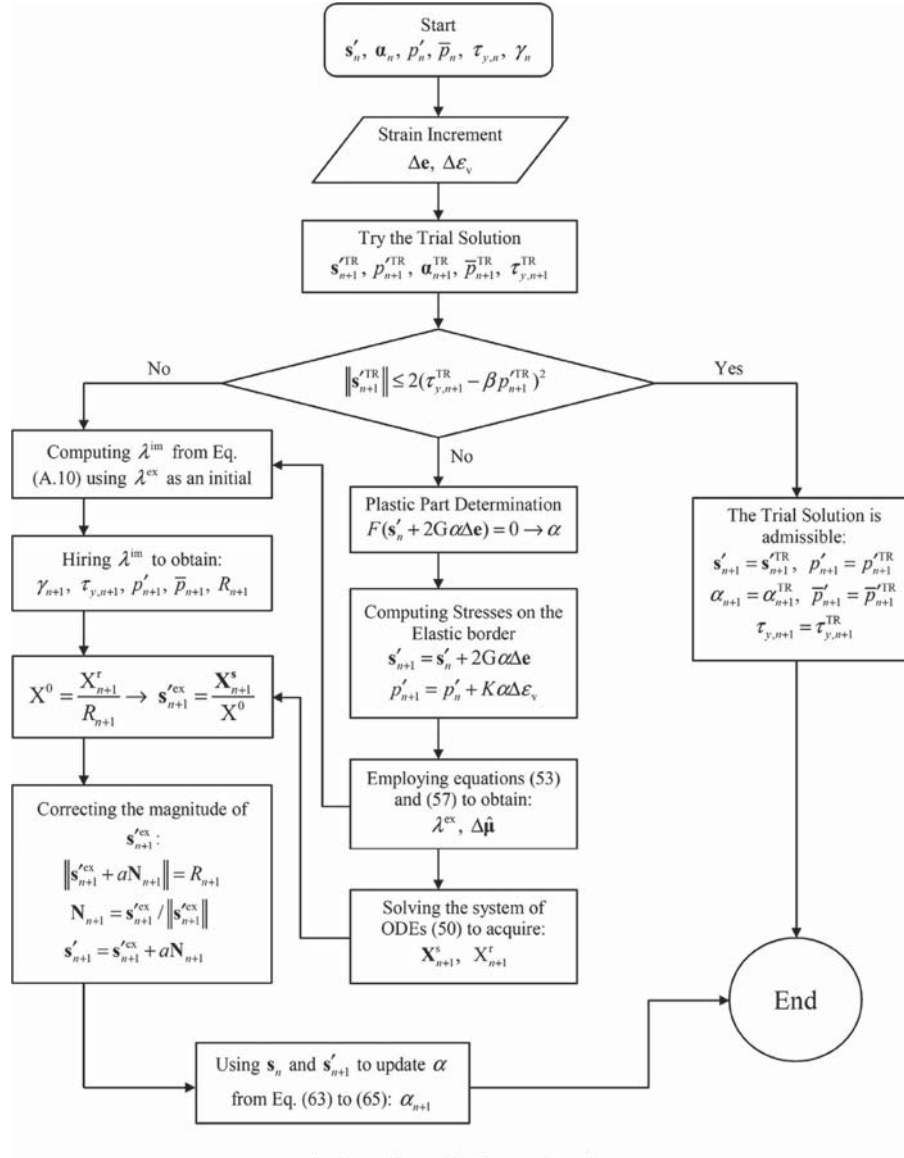
Fig. 1. The flow chart of the integrating scheme HXB.

7. Dealing with the apex

The tipping point of the Drucker–Prager cone is controversial. Once the loading history pushes the stress in the realm of the apex influence, the numerical analysis falls down. To eschew the problem, the first thing to do is to determine the apex influence realm. It means that from where exactly the stress position is critical and it requires a special treatment. This is an issue where different researchers have commented diverse tactics on, for instance, see Genna and Pandolfi [16], de Souza Neto et al. [51] and Szabo and Kossa [52]. The one used here is a straight and effective technique formed based on defining another convex set with its flank orthogonal to the main cone to which all the points inside are considered as apex influence. That is to control the following condition:

1- The stress point is outside the apex realm if $\|\mathbf{s}_{n+1}'^{TR}\| > 2G\|\Delta\mathbf{e}^p\|$;
   $\mathbf{s}_{n+1}'^{TR} = \mathbf{s}_n' + 2G\Delta\mathbf{e}$

2- The stress point is inside the apex realm if $\|\mathbf{s}_{n+1}'^{TR}\| \leq 2G\|\Delta\mathbf{e}^p\|$

The updating procedure follows its common process whenever the first condition is met while the second condition fulfillment demands different measures.

Due to the fact that, the numerical schemes introduced in this study are of explicit and implicit varieties and they really do influence the stress updating procedure, the tactic of coping with the apex singularity is separately described for each case.

7.1. Updating stress at the apex for explicit manners

Immediately, after the second condition fulfillment, the stress point gets place in the apex realm, and it must be settled on the apex. It means that

$$\mathbf{s}_{n+1}' = 0 \tag{112}$$

and

$$R_{n+1} = \sqrt{2}(\tau_{y,n+1} - \beta p'_{n+1}) = 0. \tag{113}$$

The crucial part to update the variables is to attain the discrete plastic multiplier. Here, it is important that the condition; $R_{n+1} = 0$ be utilized to compute the discrete plastic multiplier. Thus, $\tau_{y,n+1}$ and p'_{n+1} are obtained through the constitutive equations (2) and (20) following an explicit approach as

$$\tau_{y,n+1} = \tau_{y,0} + \tau_{y,s}\left[1 - \exp(-\overline{b}(\gamma_n + \lambda))\right] \tag{114}$$

$$p'_{n+1} = p'_n + K\Delta\varepsilon_v - 2\beta\lambda\overline{K}(\tau_{y,n} - \beta p'_n) + \sum_{i=1}^{m} H_{\mathrm{nl},i}\lambda\overline{p}_{n,i} \tag{115}$$

Substituting the preceding relationships, Eqs. (114) and (115), in Eq. (113) leads to an equality from which the discrete plastic multiplier must be acquired. Since the resultant is nonlinear with respect to λ, it demands a numerical procedure, such as the Newton–Raphson method, be applied in order to solve it. With the discrete plastic multiplier in hand, either of τ_y or p' could be updated through Eqs. (114) and (115), however it had better compute the other from the coming connection to have a consistent algorithm.

$$p'_{n+1} = \frac{\tau_{y,n+1}}{\beta} \tag{116}$$

Subsequently, the hydrostatic part of the back stress is readily updated using Eq. (23) with the next appearance:

$$\overline{p}_{n+1} = \overline{p}_n + \sum_{i=1}^{m}\left(\frac{2}{3}H_{\mathrm{kin},i}\lambda\beta(\tau_{y,n} - \beta p'_n) - \lambda H_{\mathrm{nl},i}\overline{p}_{n,i}\right) \tag{117}$$

Based on the following relationship, the back stress deviator is vital to update the deviatoric stress:

$$\mathbf{s}_{n+1} = \mathbf{s}'_{n+1} + \boldsymbol{\alpha}_{n+1} \tag{118}$$

Regarding the constitutive equation (7), here, the only unknown parameter is the plastic strain evolution. This could be computed via two diverse ways. One is simply to use the flow rule along with the yield function to come up with

$$\dot{\mathbf{e}}^{\mathrm{p}} = \dot{\gamma}\frac{\partial F}{\partial\mathbf{s}'} = \dot{\gamma}\mathbf{s}' \rightarrow \Delta\mathbf{e}^{\mathrm{p}} = \lambda\mathbf{s}'_n, \tag{119}$$

which is not as much accurate, and the other is to utilize the constitutive equations (19) and (10) to reach

$$\mathbf{s}'_{n+1} = \mathbf{s}'_n + 2G\Delta\mathbf{e} - \left(2G + \sum_{i=1}^{m}H_{\mathrm{kin},i}\right)\Delta\mathbf{e}^{\mathrm{p}} + \sum_{i=1}^{m}H_{\mathrm{nl},i}\lambda\boldsymbol{\alpha}_{n,i}. \tag{120}$$

In this equality, $\mathbf{s}'_{n+1}$ vanishes for being at the apex realm, the expression $2\overline{G}$ is substituted for $2G + \sum_{i=1}^{m}H_{\mathrm{kin},i}$ according to the definition in Eq. (21), and the statement $\mathbf{s}'_n + 2G\Delta\mathbf{e}$ is replaced with $\mathbf{s}'^{\mathrm{TR}}_{n+1}$. This will potentially lead to the next relationship for the evolution of the plastic strain:

$$\Delta\mathbf{e}^{\mathrm{p}} = \frac{1}{2\overline{G}}\left(\mathbf{s}^{\mathrm{TR}}_{n+1} - \boldsymbol{\alpha}_n + \lambda\sum_{i=1}^{m}H_{\mathrm{nl},i}\boldsymbol{\alpha}_{n,i}\right) \tag{121}$$

Plainly, the second manner for updating $\Delta\mathbf{e}^{\mathrm{p}}$ is more precise.

7.2. Updating stress at the apex for implicit manners

When the shifted stress occurs at the apex influence, it is essential that the same procedure as described in equalities (112)–(116) be followed even though the expression for p'_{n+1} must be modified complying with an implicit approach. Therefore, the hydrostatic shifted stress has the following formula obtained from Eqs. (20) and (23):

$$p'_{n+1} = p'^{\mathrm{TR}}_{n+1} + \lambda\sum_{i=1}^{m}\frac{H_{\mathrm{nl},i}\overline{p}_{n,i}}{1 + \lambda H_{\mathrm{nl},i}} \tag{122}$$

The described process gives rise to the coming equality from which the discrete plastic multiplier should be calculated with the
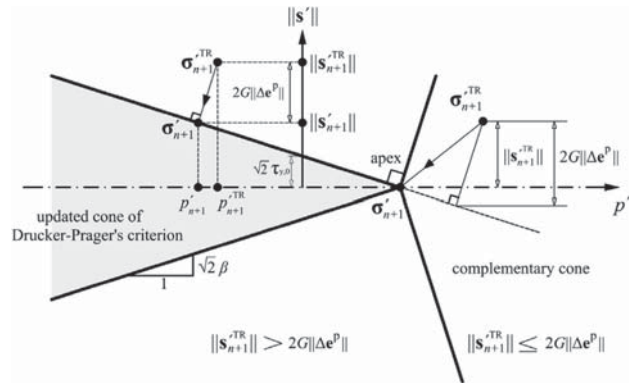
Fig. 2. Stress updating process at the apex realm.

help of a numerical solver such as Newton–Raphson procedure:

$$\tau_{y,0} + \tau_{y,s} - \tau_{y,s}\exp(-\overline{b}\gamma_n)\exp(-\overline{b}\lambda) - \beta p'^{\mathrm{TR}}_{n+1} - \beta\lambda\sum_{i=1}^{m}\frac{H_{\mathrm{nl},i}\overline{p}_{n,i}}{1 + \lambda H_{\mathrm{nl},i}} = 0 \tag{123}$$

Following an implicit manner, the deviatoric back stress is obtained through the coming relationship via Eqs. (7) and (14):

$$\boldsymbol{\alpha}_{n+1} = \sum_{i=1}^{m}\frac{\boldsymbol{\alpha}_{n,i}}{1 + \lambda H_{\mathrm{nl},i}} \tag{124}$$

Now that the discrete plastic multiplier is clear, the remaining parameters are conveniently updated using their associated constitutive equations along with taking an implicit treatment. The shear stress is updated the same as Eq. (114) and the hydrostatic back stress is computed as

$$\overline{p}_{n+1} = \sum_{i=1}^{m}\left(\frac{\overline{p}_{n,i}}{1 + \lambda H_{\mathrm{nl},i}}\right) \tag{125}$$

To better illustrate the issue one may find Fig. 2 helpful where the stress updating procedure is displayed schematically.

8. Consistent tangent operator

In a finite element analysis, the consistent tangent operator is needed to preserve the quadratic asymptotic convergence through the Newton–Raphson iterative procedure. Here, a brief explanation is presented for deriving the consistent tangent moduli corresponding to the numerical integrations. Linearizing stress updating method, the tangent operators are derived through the following equation:

$$\frac{\partial\boldsymbol{\sigma}_{n+1}}{\partial\varepsilon_{n+1}} = \frac{\partial\boldsymbol{\sigma}'_{n+1}}{\partial\varepsilon_{n+1}} + \frac{\partial\mathbf{a}_{n+1}}{\partial\varepsilon_{n+1}} \tag{126}$$

The present relationship is expanded to the subsequent one utilizing Eqs. (4)–(6), and (8):

$$\frac{\partial\boldsymbol{\sigma}_{n+1}}{\partial\varepsilon_{n+1}} = \left(\frac{\partial\mathbf{s}'_{n+1}}{\partial\mathbf{e}_{n+1}} + \frac{\partial\boldsymbol{\alpha}_{n+1}}{\partial\mathbf{e}_{n+1}}\right)\mathbb{I}_{\mathrm{dev}} + \left(\frac{\partial\mathbf{s}'_{n+1}}{\partial\varepsilon_{v,n+1}} + \frac{\partial\boldsymbol{\alpha}_{n+1}}{\partial\varepsilon_{v,n+1}}\right)\mathbf{i}^{\mathrm{T}}$$
$$+ \left(\frac{\partial p'_{n+1}}{\partial\varepsilon_{v,n+1}} + \frac{\partial\overline{p}_{n+1}}{\partial\varepsilon_{v,n+1}}\right)\mathbf{ii}^{\mathrm{T}} + \left(\frac{\partial p'_{n+1}}{\partial\mathbf{e}_{n+1}} + \frac{\partial\overline{p}_{n+1}}{\partial\mathbf{e}_{n+1}}\right)\mathbf{i}^{\mathrm{T}}\mathbb{I}_{\mathrm{dev};}$$

$$\mathbb{I}_{\mathrm{dev}} = \mathbb{I} - \frac{1}{3}(\mathbf{ii}^{\mathrm{T}}) \tag{127}$$

One could readily compute the components of the above equality referring to the relationships of $\mathbf{s}'$, $\boldsymbol{\alpha}$, p', and $\overline{p}$ given for each integration method in the related sections. Appendix C, for instance, explicitly addresses the consistent tangent modulus of the suggested hybrid integration, HXB.

9. Numerical tests

The suggested schemes are assessed in diverse grounds of accuracy, efficiency, and convergence rate. The appraisal is based on comparative investigations between the proposed formulations and the well-known techniques of the Forward Euler and Back ward Euler which are presented in Appendixes A and B. The results of the Euler integrations with as minute load-step sizes as $\Delta t = 1 \times 10^{-5}$ are presumed as exact solutions for the lack of them. Complying with the considered plasticity, the properties of a bainitic high strength roller bearing steel is adopted. The steels are reliable components for transmitting high loads with minimum fraction and accurate location through rotational movement [53]. The following presents the mechanical characteristics of the chosen steel as

Elastic constants of $E = 203\text{GPa}$ and $\nu = 0.27$.

Isotropic hardening characteristics as

$$\tau_{y,0} = \frac{1600}{\sqrt{3}} \text{ MPa}, \quad \tau_{y,s} = \frac{-100}{\sqrt{3}}, \quad \text{and } \bar{b} = 534.$$

Kinematic hardening properties with

$$\begin{cases} H_{\text{nl},1} = 300, \ H_{\text{nl},2} = 1000, \ H_{\text{nl},3} = 0 \\ H_{\text{kin},1} = 113.33 \text{ GPa}, \ H_{\text{kin},2} = 133.33 \text{ GPa}, \ H_{\text{kin},3} = 10 \text{ GPa} \end{cases}$$

For the sake of conciseness, the following abbreviations are used to represent the integrations:

BE: Backward Euler Integration
FE: Froward Euler Integration
EX: Exponential Map Integration
HXB: Hybrid Integration between Exponential Map and Backward Euler
EXS: Semi-Implicit Exponential Map Integration
HXF: Hybrid Integration between Exponential Map and Forward Euler

9.1. Accuracy investigation

The accuracy of an integration scheme directly influences the outcomes of a nonlinear finite element analysis. Therefore, it is crucial that the precision of the suggested formulations be evaluated with as much certitude as possible. Two reliable tools for the purpose are strain load histories and iso-error maps.

9.1.1. Strain load histories

As the most common way of investigating accuracy, the stresses are updated for a number of given strain histories using the integrating schemes under discussion. This way, the schemes are assessed while they are being used in updating the stress state at a given Gauss point, and therefore, whatever the results are they would have an accumulative effect on the outputs of a real nonlinear finite element problem. Three biaxial non-proportional strain paths along with their strain histories are adopted as shown in Figs. 3–8. The strain paths are linearly piecewise to avoid the discretization errors. Each strain history consists of two components that alter proportionally to the first yielding strain as

$$\varepsilon_{y,0} = \frac{\sqrt{3}\tau_{y,0}}{2G}, \tag{128}$$

with other strain components zero.

The accuracies of the suggested techniques are assessed using the relative errors of the updated stresses via each integration scheme. As a basis of the investigation, the stresses are also updated by Euler's tactics, so they could be compared with the new formulations. The relative or non-dimensional stress error is
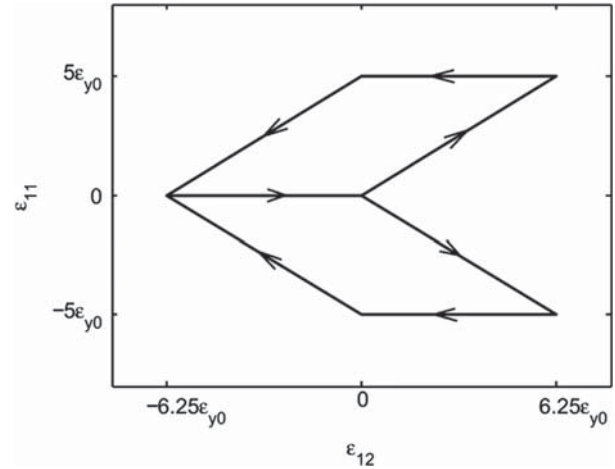
Fig. 3. Strain Path 1.
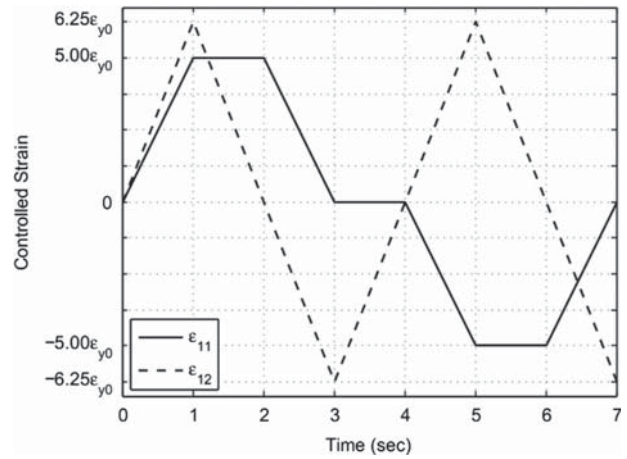
Fig. 4. Strain History 1.
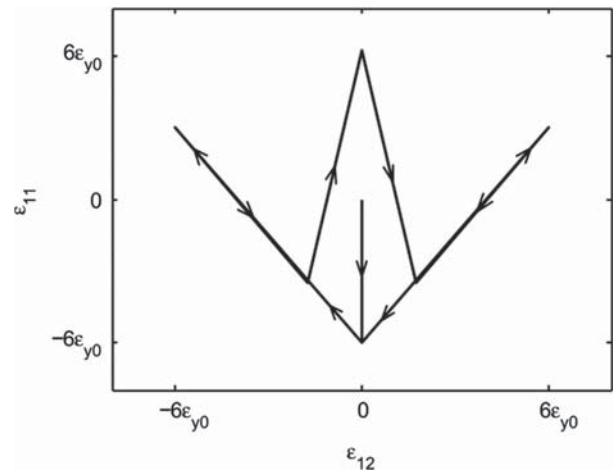
Fig. 5. Strain Path 2.

defined as

$$E_n^\sigma = \frac{\|\sigma_n - \bar{\sigma}_n\|}{\|\bar{\sigma}_n\|} \tag{129}$$
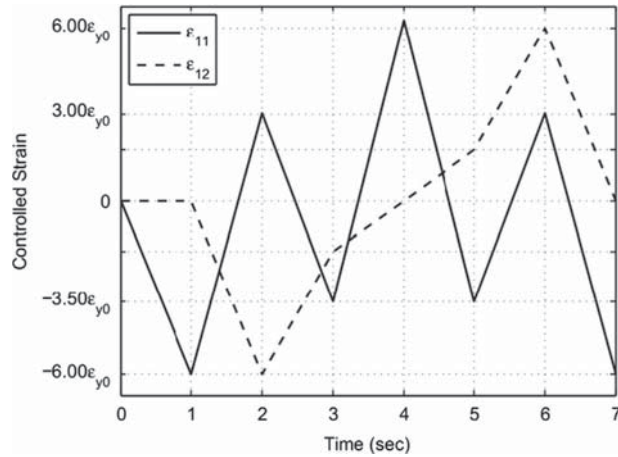
Fig. 6. Strain History 2.
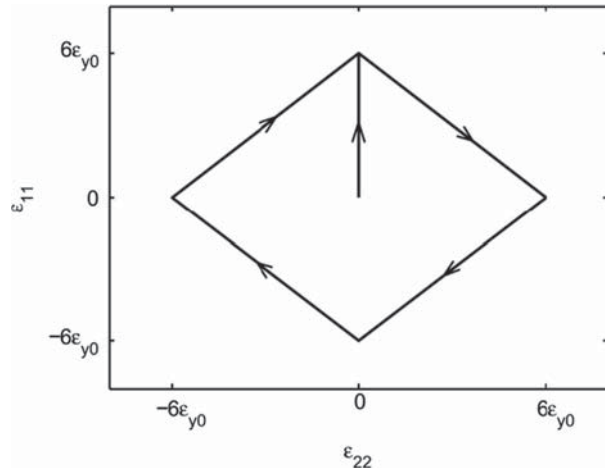
Fig. 7. Strain Path 3.
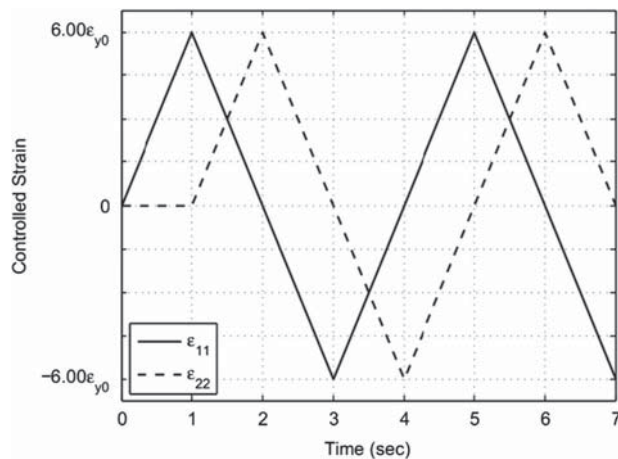
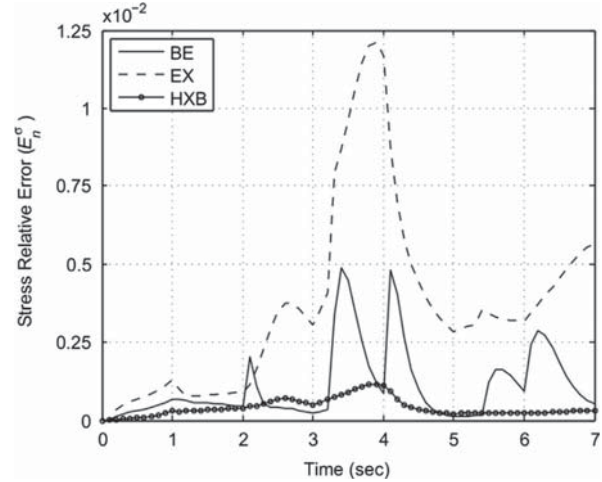**Fig. 8.** Strain History 3.

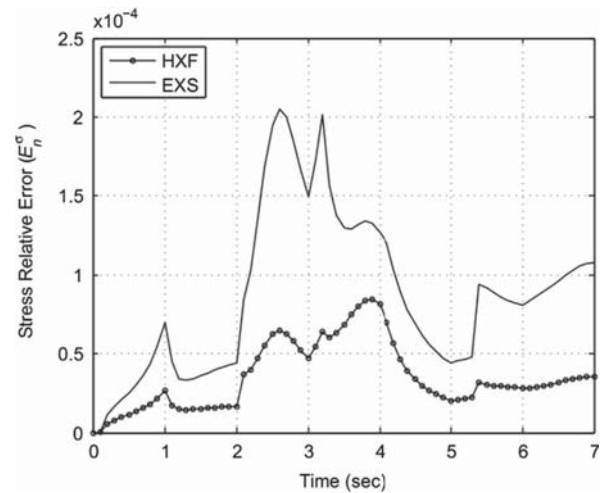**Fig. 9.** Stress errorrs of Path 1, first-order schemes $\Delta t = 0.1$s.

Fig. 10. Stress errorrs of Path 1, second-order schemes $\Delta t = 0.1$s.
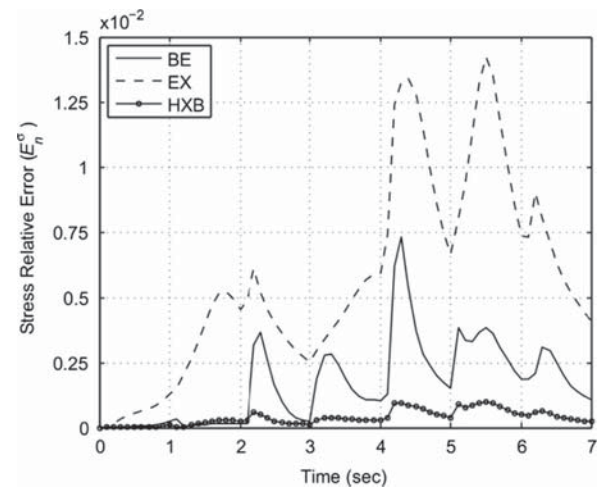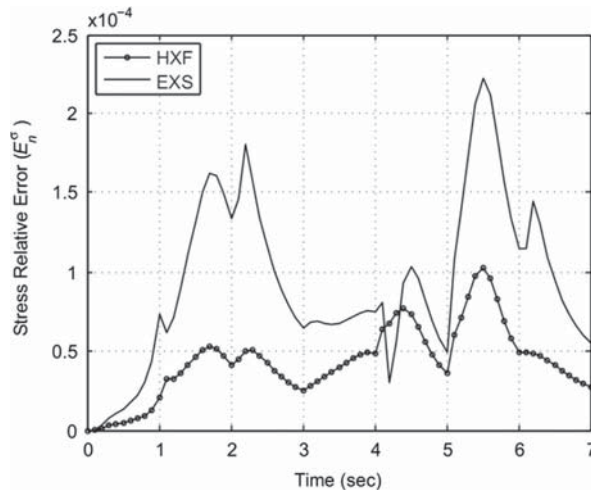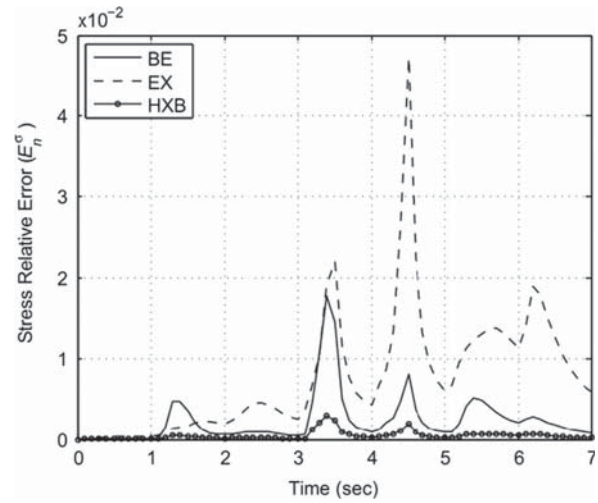

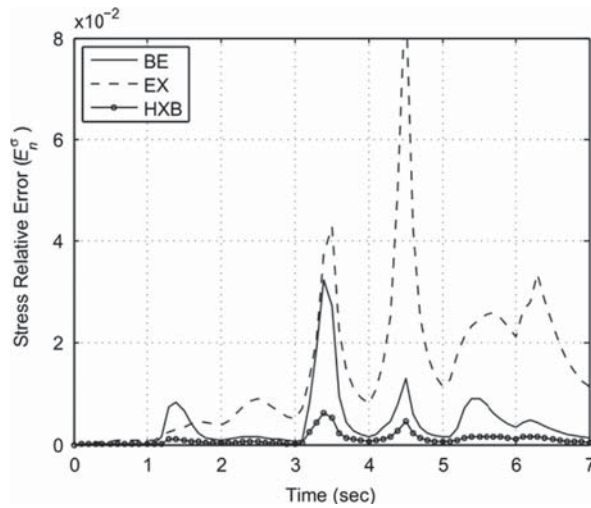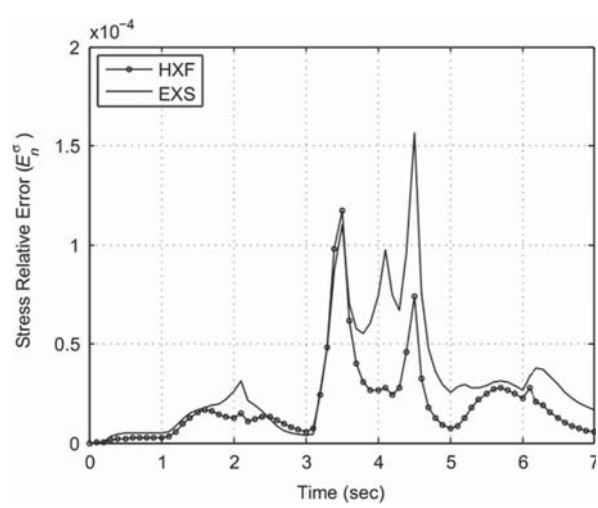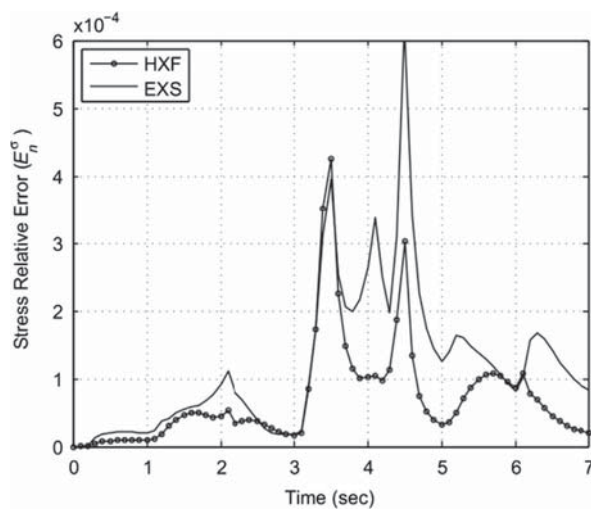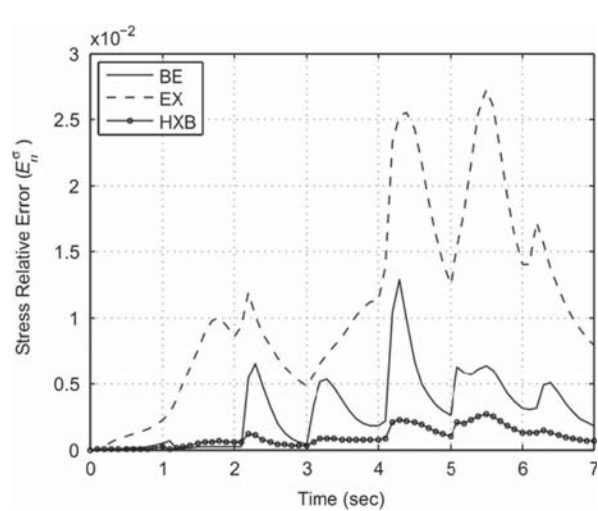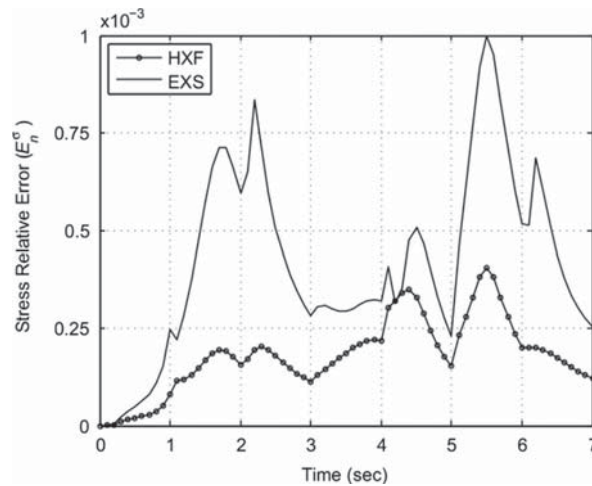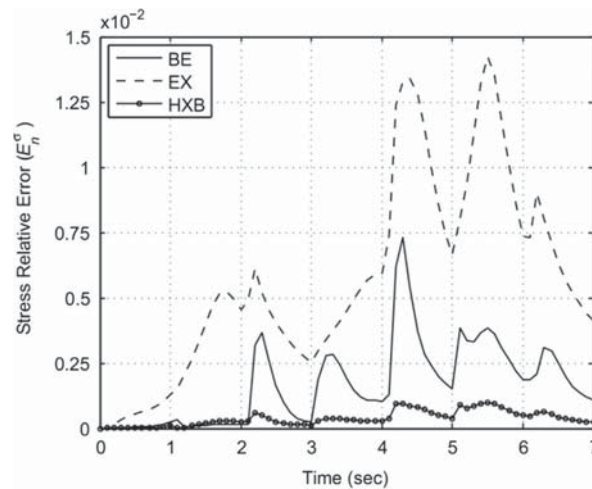**Fig. 11.** Stress errorrs of Path 1, first-order schemes $\Delta t = 0.05$s.

where $\bar{\sigma}_n$ stands for the exactly updated stress at time t_n and σ_n shows the stress vector corresponding to the time t_n. The comparison is carried out for two practical strain increments of $\Delta t = 0.1$ and 0.05**s**. Figs. 9–20 present a broad set of comparisons between the proposed integrations and Euler's.

Before proceeding the investigation, some considerations are needed. First of all, the Forward Euler integration is of no accuracy as if its precision is about ten times weaker than BE owing mostly to

Fig. 12. Stress errorrs of Path 1, second-order schemes $\Delta t = 0.05$s.

Fig. 15. Stress errorrs of Path 2, first-order schemes $\Delta t = 0.05$s.

Fig. 13. Stress errorrs of Path 2, first-order schemes $\Delta t = 0.1$s.

Fig. 16. Stress errorrs of Path 2, second-order schemes $\Delta t = 0.05$s.

Fig. 14. Stress errorrs of Path 2, second-order schemes $\Delta t = 0.1$s.

Fig. 17. Stress errorrs of Path 3, first-order schemes $\Delta t = 0.1$s.
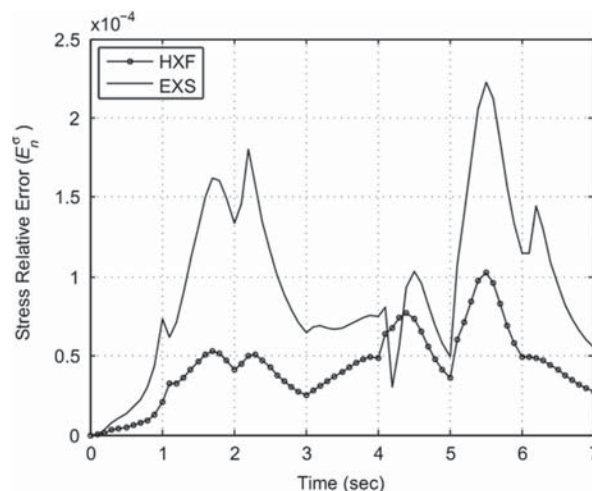
Fig. 18. Stress errorrs of Path 3, second-order schemes $\Delta t = 0.1$s.

the shape of the yield surface and the nonlinear isotropic hardening causing dramatic changes in the yield surface radius. This will demand the presence of the FE be disregarded favoring the investigation, for instance see Figs. 21 and 22. Additionally, of all four integrations suggested, the EX and HXB come with first-order rate of convergence whereas the EXS and HXF are second-order schemes, as it will be demonstrated in the Convergence Rate section. Thus, the two latter cases have such an accuracy their stress-error graphs cannot be displayed conceivably in a single diagram with the associated first-order integrations. This will mandate separate figures for each class.

Overall, the HXF and HXS are the most accurate schemes in the group owing mostly to their convergence rate. They have accuracy of second-order while the others are all first-order schemes. Moreover, the HXF is more precise than EXS based on Figs. 10, 12, 14, 16, 18 and 20. The reason is that the EX and FE cover their drawbacks through the suggested scheme, HXF, for converging to the response via two different directions. Amid the first order schemes, the proposed HXB is far more accurate than EX and BE according to Figs. 9, 11, 13, 15, 17, and 19. The HXB is almost ten times more precise than EX and three times relative to BE.

Fig. 19. Stress errorrs of Path 3, first-order schemes $\Delta t = 0.05$s.
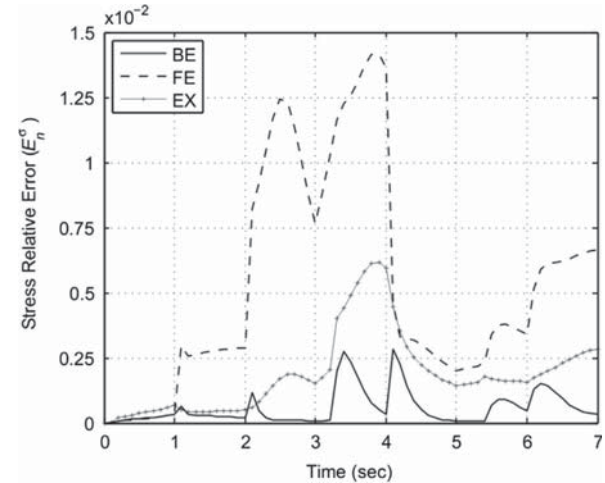
Fig. 21. Demonstration of rough accuracy of FE Strain Path 1, $\Delta t = 0.05$s.

Fig. 20. Stress errorrs of Path 3, second-order schemes $\Delta t = 0.05$s.
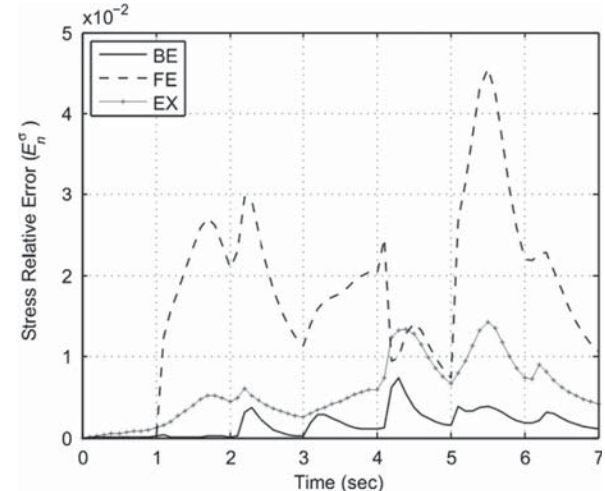
Fig. 22. Demonstration of rough accuracy of FE Strain Path 3, $\Delta t = 0.05$s.

9.1.2. Iso-error maps

Evaluating the accuracy of three numerical integrations along with an exact one, Krieg and Krieg [5] first devised iso-error maps. Since then, a growing number of scientists have adopted the technique in their studies, such as Ortiz and Popov [8], Ortiz and Simo [54], Loret and Prevost [13], Genna and Pandolfi [16], Simo and Hughes [55], Artioli et al. [32,33], de Souza Neto et al. [51], Rezaiee Pajand et al. [50] and so on. Today, the iso-error maps are known as a methodical robust way to examine the precision of plasticity integrations.

The error contours are acquired for a purely plastic step where the deviatoric strain increment is of arbitrary amplitude but have the same principle direction as $\mathbf{s}'_C$or$\mathbf{s}'_{n+\alpha}$. This will ease the precision investigation and help it be conveniently visualized in the deviatoric plane with least influence on the general conclusions. The dilatancy parameter V is defined as the ratio of the hydrostatic to deviatoric parts of the strain increment to specify the total strain evolution $\Delta\varepsilon$. As the basis of the deviatoric stress plane, the orthonormal system of $(\hat{n}, \hat{t})$ is hired where $\hat{n}$ is the normal unit outward to the yield surface at $\mathbf{s}'_{n+\alpha}$, and it is defined as

$$\hat{n} = \frac{\mathbf{s}'_n}{\|\mathbf{s}'_n\|} = \frac{\mathbf{s}'_n}{R_n} \tag{130}$$

The direction and amplitude of the deviatoric loading increment are readily identified through the following radial and tangential projections:

$$N = \frac{2\sqrt{2}G}{R_n}\|\Delta\mathbf{e}\|\cos(\psi_n) \tag{131}$$

$$T = \frac{2\sqrt{2}G}{R_n}\|\Delta\mathbf{e}\|\sin(\psi_n) \tag{132}$$

where ψ_n is the angle between the deviatoric loading increment and the normal $\hat{n}$, see Fig. 23.

The accuracy of the integration algorithms is investigated through the two diverse grounds of orientation and the amplitude assessments of the final stress. The evaluation is carried out utilizing the angular error:

$$\Delta\theta = \cos^{-1}\left(\frac{(\mathbf{s}'^{E}_{n+1})^{T}\mathbf{s}'_{n+1}}{R^{E}_{n+1}R_{n+1}}\right) \tag{133}$$

and the radial error:

$$\Delta R = \left(1 - \frac{R_{n+1}}{R^{E}_{n+1}}\right), \tag{134}$$

in which $\mathbf{s}'^{E}_{n+1}$ and R^{E}_{n+1} stand for the exact solution of the deviatoric shifted stress computed through one of Euler's scheme

with a very fine load-step size. And $\mathbf{s}'_{n+1}$ and R_{n+1} represent the approximate results by the algorithms. An illustration of these errors is presented in Fig. 24. The investigation is performed over the rectangular domain of

$$-5 \leq N \leq 5, \quad 0 \leq T \leq 5 \tag{135}$$

Two particular amounts of $V = 0$ and $V = 1$ are adopted for the dilatancy parameter. In case of $V = 0$, the angle ψ_n could vary only between 0 and $\pi/2$ ensuring that the stress stay in the plastic phase. This will demand the parameter N take the limited domain of $0 \leq N \leq 5$. Nonetheless, where there be the $V = 1$, the trial stress does not extend across the yield surface for laying tangentially on the convex set and therefore the domains of $0 \leq \psi_n \leq \pi$ and $-5 \leq N \leq 5$ are expected to happen, see Figs. 25–28.

In essence, the proposed schemes are all based on the three well-known integrations of BE, FE, and EX. Consequently, to best interpret the associated iso-error contours, one needs to comprehensively perceive the behavior of these basic methods. The explicit techniques of FE and EX are apparently quite competent whenever the yield surface radius has the least variation. The realization of this fact is best beheld in the case of $V = 0$, according to Figs. 31–34, where loading occurs in π – plane with least sign of change in R.

In such circumstances, the EX appears superior to FE and BE and, as a result, the second-order scheme totally based on the exponential map, i.e. EXS, has the least angular and radial errors as Figs. 37 and 38 prove it. Though, the problem with the explicit integrations arises when R starts to change during a loading process which is also very likely in a real condition. This aggravates
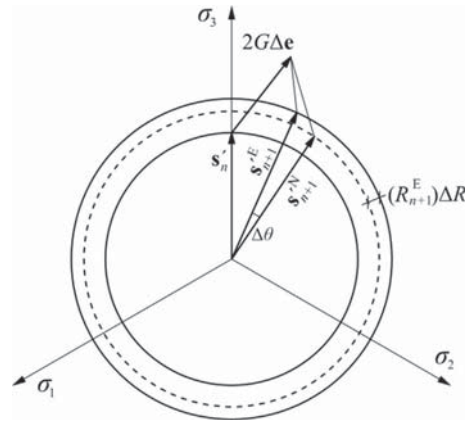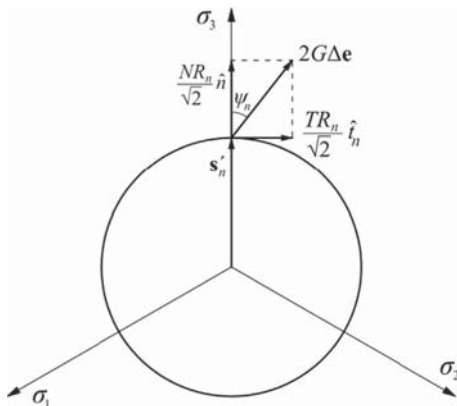
Fig. 24. Illustration of the radial and angular errors.

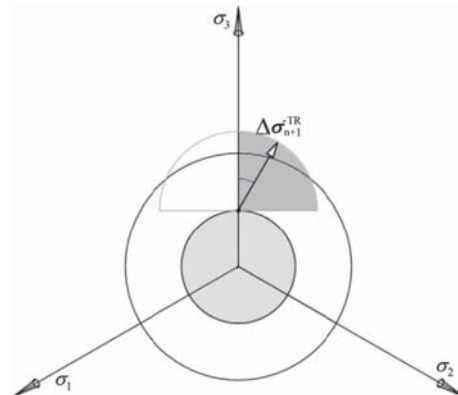**Fig. 23.** Definition of the parameters N and T.

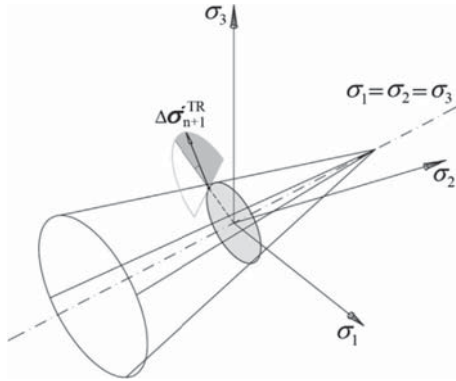**Fig. 25.** The trial stress state in the deviatoric plane, $V = 0$.

Fig. 26. The trial stress state in the space of principle stresses, $V = 0$.
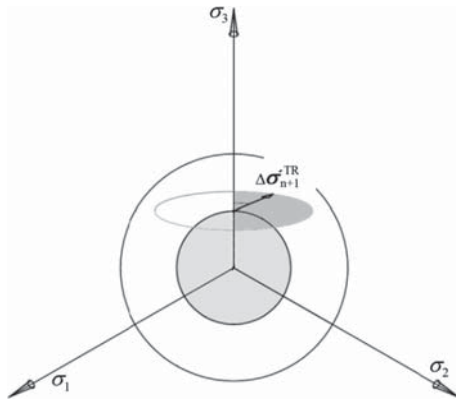

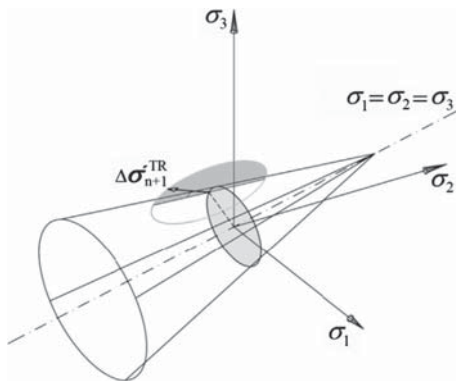**Fig. 27.** The trial stress state in the deviatoric plane, $V = 1$.

Fig. 28. The trial stress state in the space of principle stresses, $V = 1$.

Fig. 29. The angular error of BE for $V = 0$.

Fig. 30. The radial error of BE for $V = 0$.

Fig. 31. The angular error of FE for $V = 0$.

most, according to the isodiagrams of Figs. 43–46, when it comes to extreme cases of radius alterations in $V = 1$ in which even FE shows a better performance than EX. This will contribute to the supremacy of HXF towards EXS, especially in the case of radial errors as observed in Figs. 49–52.

Referring to Figs. 41 and 42, obviously, the state of $V = 1$ is the area of expertise of Backward Euler in which BE is essentially proficient in computing the yield surface radius alongside preserving a good accuracy in finding the stress directions. Here, the merely major drawback of BE is when loading history induces considerable changes in stress direction as if surfaces most in its angular error of $V = 0$, see Figs. 29 and 30. This problem with BE and also the deficiency of EX in figuring the yield surface radius are all eradicated in HXB. Having every vantage of BE and EX, the
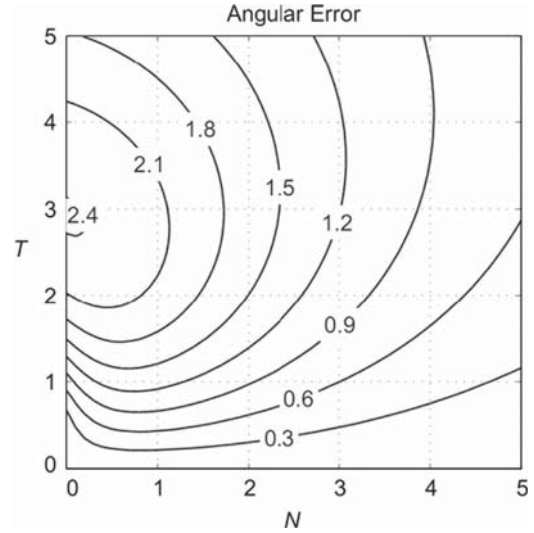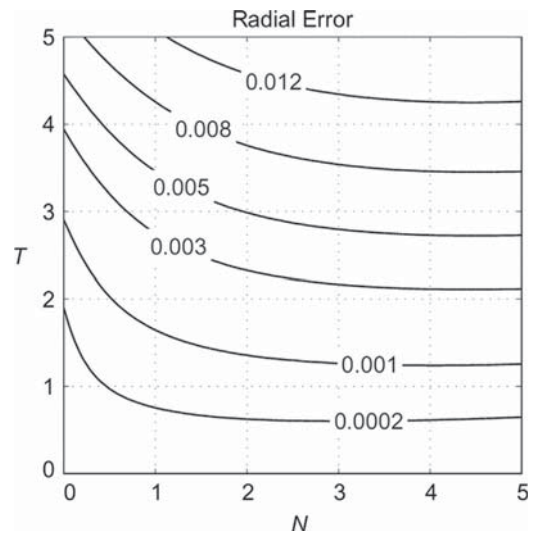
Fig. 32. The radial error of FE for $V=0$.

Fig. 35. The angular error of HXB for $V=0$.
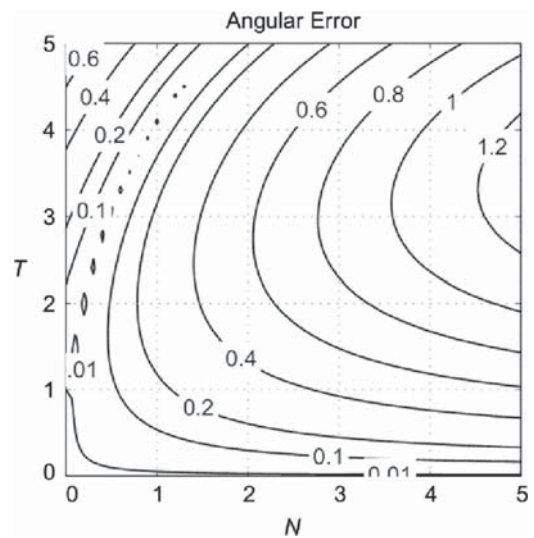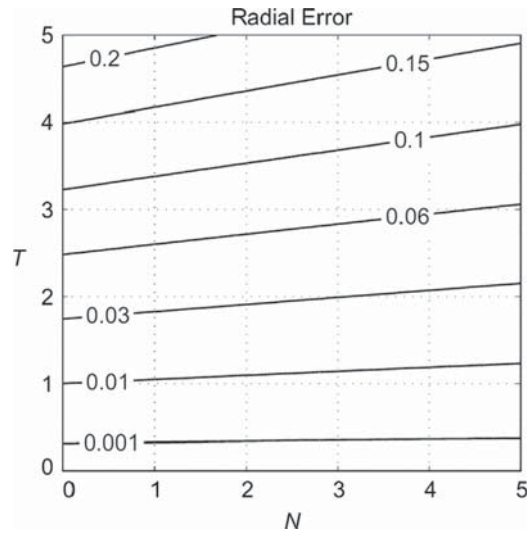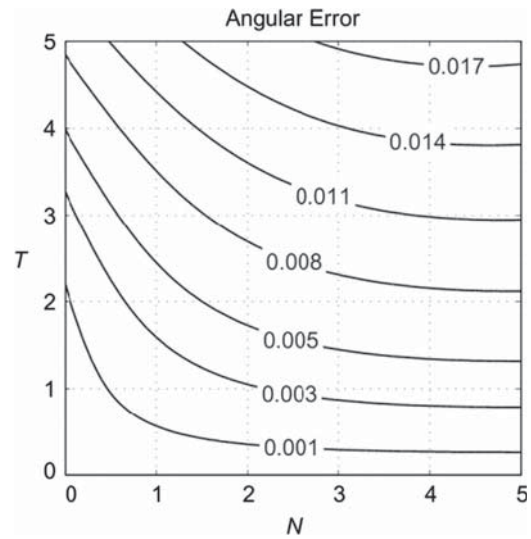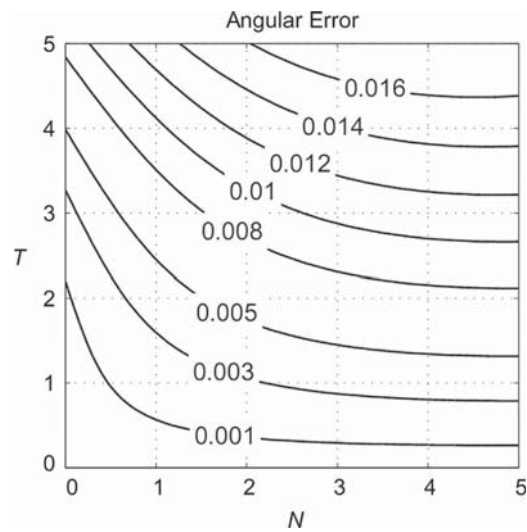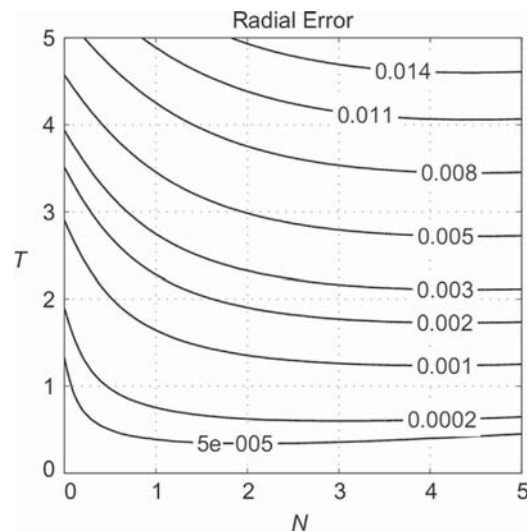

Fig. 33. The angular error of EX for $V=0$.

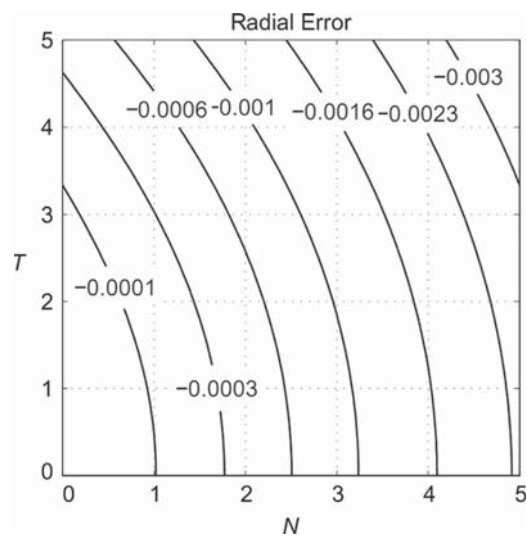Fig. 36. The radial error of HXB for $V=0$.

Fig. 34. The radial error of EX for $V=0$.

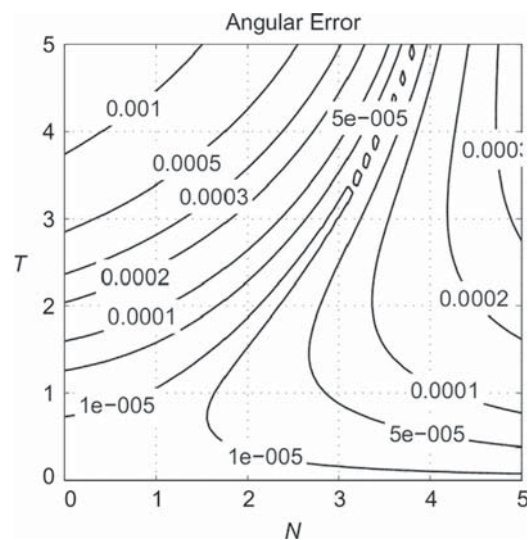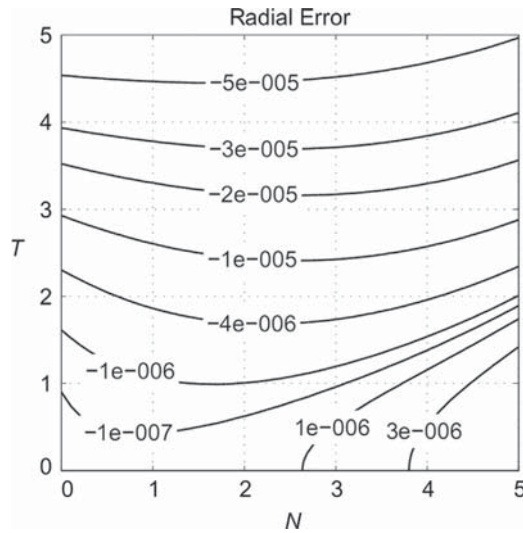Fig. 37. The angular error of EXS for $V=0$.

Fig. 38. The radial error of EXS for $V = 0$.

Fig. 41. The angular error of BE for $V = 1$.

Fig. 39. The angular error of HXF for $V = 0$.

Fig. 42. The radial error of BE for $V = 1$.

Fig. 43. The angular error of FE for $V = 1$.

Fig. 40. The radial error of HXF for $V = 0$.

Fig. 44. The radial error of FE for $V = 1$.

Fig. 45. The angular error of EX for $V = 1$.

Fig. 46. The radial error of EX for $V = 1$.
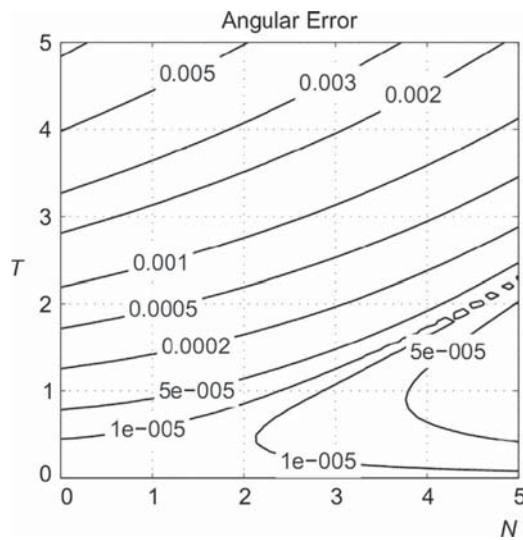
Fig. 47. The angular error of HXB for $V = 1$.
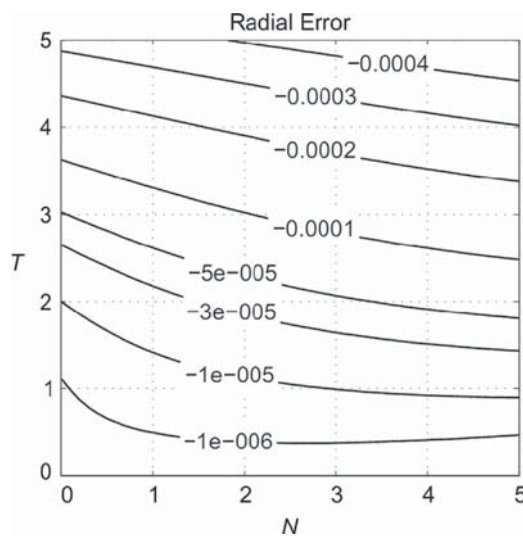
Fig. 48. The radial error of HXB for $V = 1$.
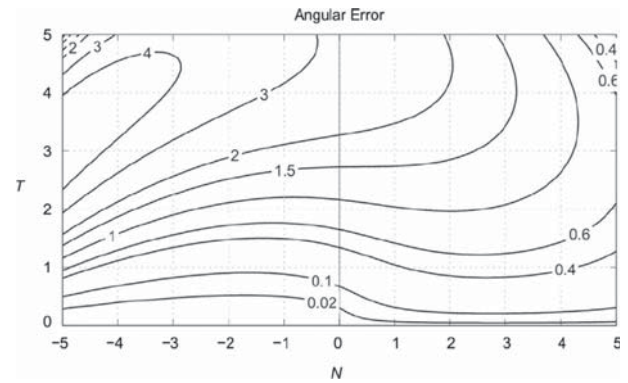
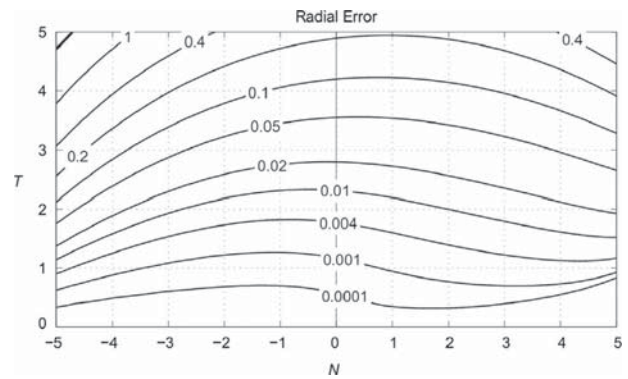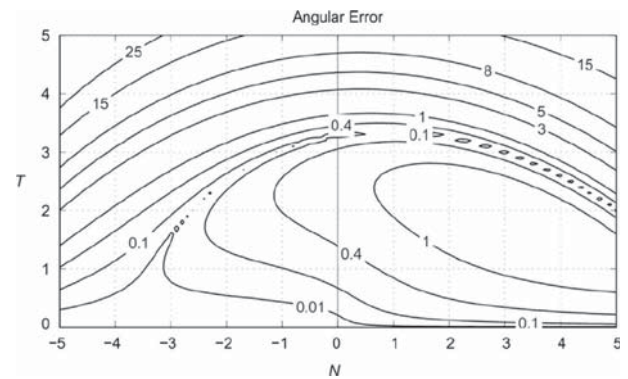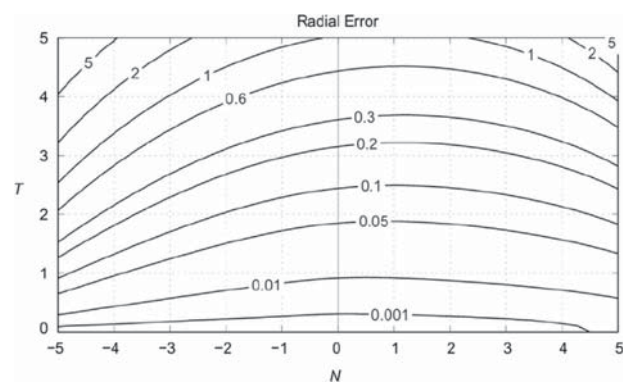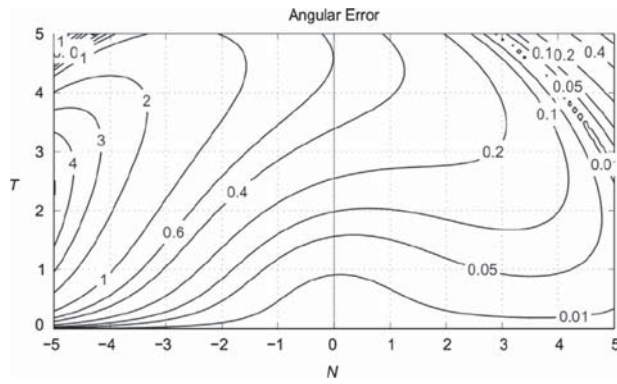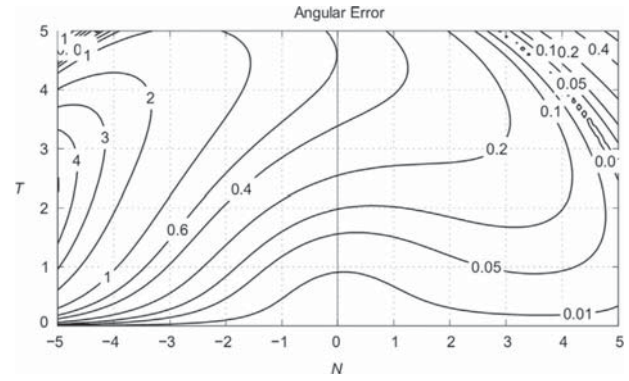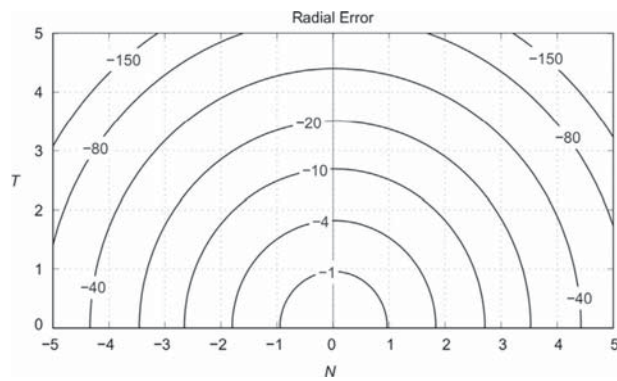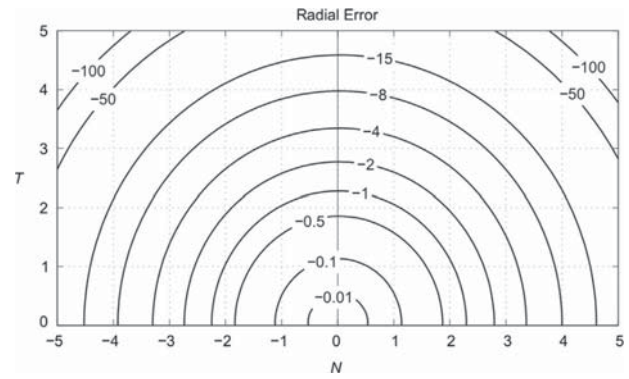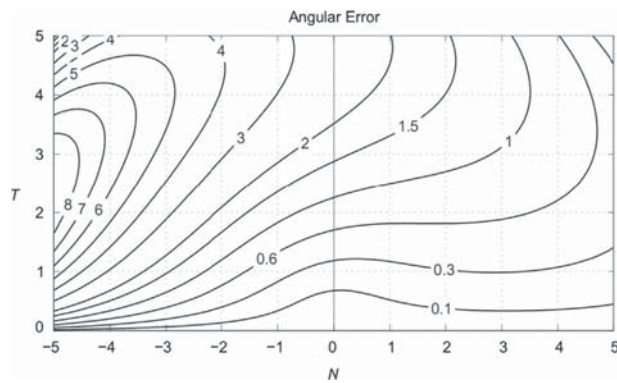**Fig. 49.** The angular error of EXS for $V = 1$.

Fig. 50. The radial error of EXS for $V = 1$.
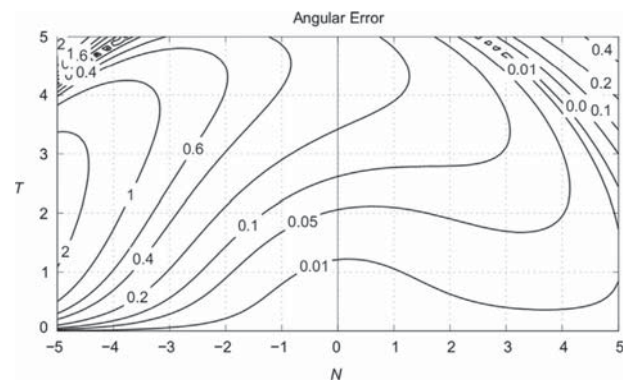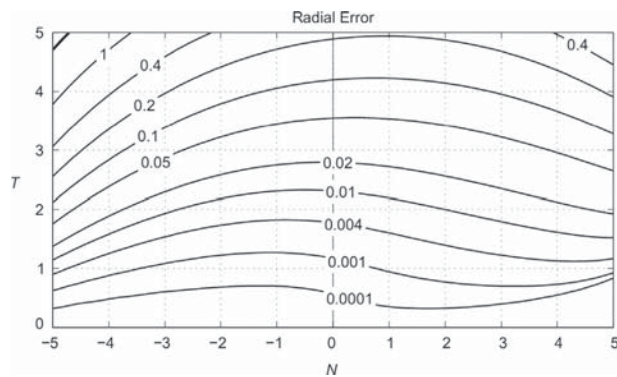
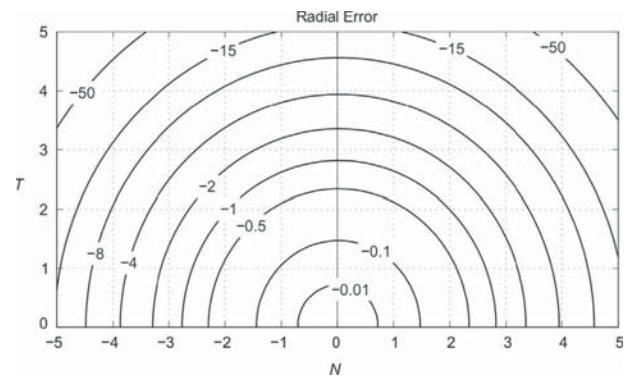**Fig. 51.** The angular error of HXF for $V = 1$.

Fig. 52. The radial error of HXF for $V = 1$.

HXB has the lowest angular and radial errors among the first-order schemes regarding Figs. 35, 36, 39, 40, 47, and 48.

In sum, the second-order integrations, i.e. EXS and HXF, are in much better precision than FE, BE, and EX, and to some extent than HXB, mostly because of their convergence rate. HXF and EXS have convergence rate of order 2 while the rest are first-order. Generally, HXF presents better accuracy than EXS. Among the first order schemes, HXB always is way more precise than FE, EX, and BE either in $V = 0$ or $V = 1$.

9.2. Efficiency investigation

An undeniable fact of the numerical integrations is that for the most part they could get to the same responses as each other but at different efforts and times, some with less efforts and as a result sooner and some later. At this study, for instance, the forward Euler integration, which was demonstrated as the least accurate one, could update the stresses with similar precision as others only if the chosen load-step size was fine enough, for example 5 times smaller. Hence, it is crucial that both accuracy and computational time be taken into account when examining a numerical method. Consequently, the numerical integrations need to be investigated in case of efficiency as a measure of effectiveness with which the numerical integrations perform.

To assess the efficiency of the integrations in question, the computational efforts are compared to each other when achieving the same accuracy. Table 1 yields the comparison where the CPU times recorded during the stress-updating procedures by each scheme are presented for a given precision. Note that, the stresses

Table 1
Computational time of the schemes for 60 cycles of the strain Histories 1 and 2.

Integration scheme	Stress History 1		Strain History 2	
	Total error	CPU time (s)	Total error	CPU time (s)
HXF	0.149	1.66	0.299	1.62
EXS	0.148	3.63	0.297	2.98
HXB	0.147	35.44	0.291	26.62
BE	0.148	96.52	0.297	178.82
EX	0.149	132.69	0.297	274.81
FE	0.147	114.85	0.296	280.21

are updated for 60 cycles of strain histories 1 and 2 to more accurately record the CPU times.

Based on the table, the EXS and HXF are much more efficient than the first-order schemes mainly for their second-order convergence rate. In their midst, the efficiency of HXF is about two times more than the EXS owing to greater accuracy besides superior speed. Among the first-order schemes, the HXB is way more efficient than the others while BE displays a better performance compared to the EX and FE having relatively equal efficiency. The reason is the greater accuracy of HXB along with its reasonable speed which is approximately 20% faster than BE.

9.3. Convergence rate

To best verify the convergence rate of the suggested algorithms, first their stress relative errors are plotted for a succession of load-step sizes from 0.1 to 0.0125 and then the average stress errors of the new and classical schemes are logarithmically graphed against each other. This way, the realms and rates of the convergence of

Fig. 54. Stress relative errors of HXB in a succession of load step sizes for strain History 1.

Fig. 53. Stress relative errors of EX in a succession of load step sizes for strain History 1.

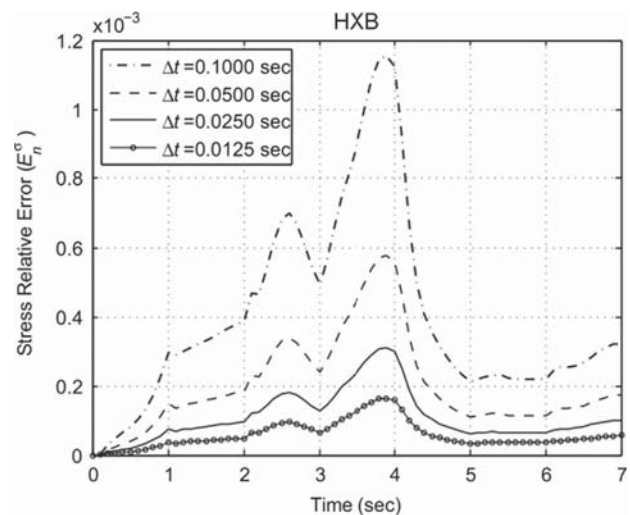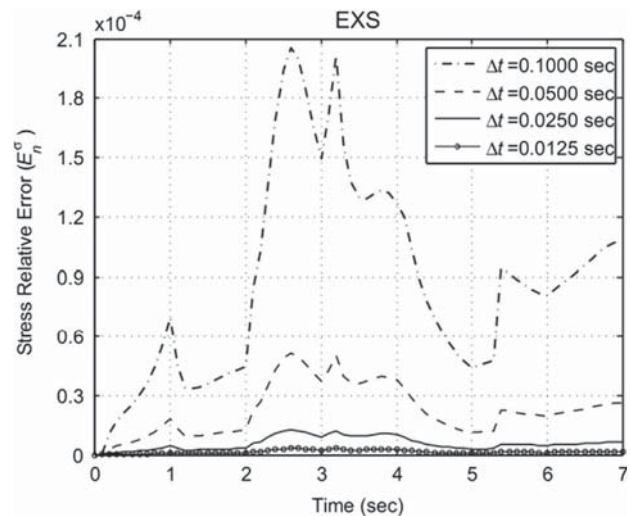**Fig. 55.** Stress relative errors of EXS in a succession of load step sizes for strain History 1.
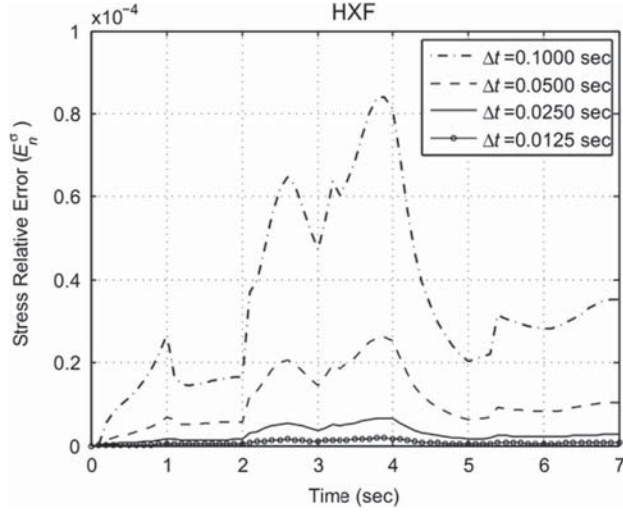
Fig. 56. Stress relative errors of HXF in a succession of load step sizes for strain History 1.
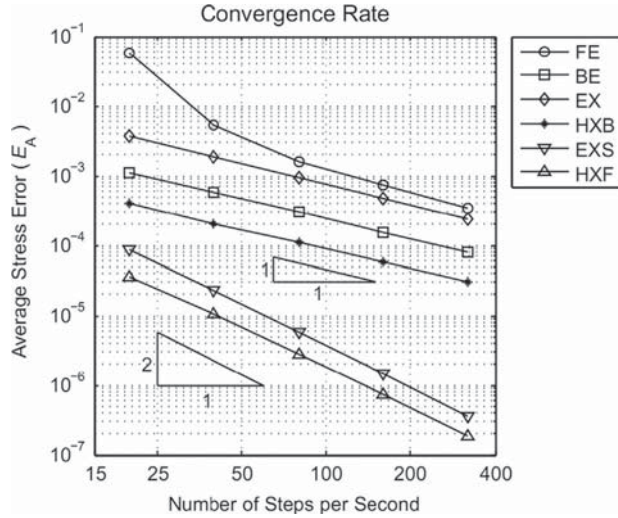

Fig. 57. The proof of convergence rate of the schemes in question.

the schemes are clearly presented. Since the behavior is the same for any kinds of loading histories regarding the test, the graphs are drawn up only for one of the strain paths to avoid lengthening, see Figs. 53–57. According to the diagrams, especially Fig. 57, the EX and HXB illustrate a linear convergence rate the same as Euler's. The FE displays some instability with large load increments, which in this example ends at $\Delta t = 0.025$, despite others. The quadratic convergence rate for EXS and HXF is clearly descried contributing to a very fast convergence to the exact solution.

10. Conclusion

In this study, two new hybrid integrations, HXB and HXF, were proposed based on the exponential map and Euler's algorithms. The schemes were developed for the general nonlinear plasticity of Drucker–Prager yield criterion with Chaboche's nonlinear isotropic and kinematic hardenings. Two exponential-based integrations, EX and EXS, were also derived for the plasticity to be compared to the suggested algorithms. Besides, dealing with the apex of the Drucker–Prager cone was described for the generic approaches of implicit and explicit integrations.

Subsequently, the derived integrations of EX and EXS along with the proposed hybrid schemes were examined in a series of numerical tests comprising accuracy, efficiency, and convergence rate investigations. To expand the investigation to a more general state, the classical integrations of Backward Euler, BE, and Forward Euler, FE, were also included in the tests. The schemes in question have two different rates of convergence; FE, BE, EX, and HXB are first-order tactics while EXS and HXF are second-order. Among the first-order schemes, the suggested HXB presents great accuracy and efficiency, which is much better than FE, BE and EX. The BE displays a better accuracy and efficiency than EX and FE. The better precision of EX over FE is overshadowed by greater speed of FE, which contributes to approximately the same efficiencies as each other. Moreover, amid the second-order strategies, the HXF demonstrates superior performance over EXS as it is nearly 25% more precise and 200% more efficient than it. Regarding the first-order and second-order methods, the HXF and EXS are unconditionally more accurate and efficient than the BE, FE, EX, and HXB. Eventually, the stress relative errors of the schemes were graphed for a succession of load-step sizes to verify the convergence rates of the integrations under discussion.

Appendix A. Backward Euler integration

This is to briefly present the Backward Euler integration for the plasticity model. Following an implicit manner, the unknown quantities at the end of the time step are used to draw the necessary relationships. First, an elastic trial as in the following equation is imposed which is followed by deducting the plastic part if involves:

$$\mathbf{s}_{n+1}^{\mathrm{TR}} = \mathbf{s}_n + 2G\Delta\mathbf{e}; \quad \boldsymbol{\alpha}_{n+1}^{\mathrm{TR}} = \boldsymbol{\alpha}_n; \quad p'^{\mathrm{TR}}_{n+1} = p'_n + K\Delta\varepsilon_{\mathrm{v}}$$

$$\bar{p}_{n+1}^{\mathrm{TR}} = \bar{p}_n; \quad \tau_{y,n+1}^{\mathrm{TR}} = \tau_{y,n} \tag{A.1}$$

For the trial solution to be admissible, the condition,

$$\|\mathbf{s}'^{\mathrm{TR}}_{n+1}\| \le R_{n+1}^{\mathrm{TR}} = \sqrt{2}(\tau_{y,n+1} - \beta p'^{\mathrm{TR}}_{n+1}), \tag{A.2}$$

must be satisfied. Otherwise, the tentative outcomes are rejected meaning a plastic corrector is required. In the latter case, coming approach is executed to update the needed values. The following parameters are defined to simplify the equations to come:

$$C_{1,i} = \frac{H_{\mathrm{kin},i}H_{\mathrm{nl},i}}{1 + H_{\mathrm{nl},i}\lambda}, \quad C_{2,i} = \frac{H_{\mathrm{nl},i}}{1 + H_{\mathrm{nl},i}\lambda} \tag{A.3}$$

$$C_{3,i} = \frac{1}{1 + H_{\mathrm{nl},i}\lambda}, \quad C_{4,i} = \frac{H_{\mathrm{kin},i}}{1 + H_{\mathrm{nl},i}\lambda} \tag{A.4}$$

Equations Eqs. (7) and (14) are utilized to acquire the deviatoric back stress as

$$\boldsymbol{\alpha}_{n+1} = \sum_{i=1}^{m} \boldsymbol{\alpha}_{n+1,i} \quad \text{with} \quad \boldsymbol{\alpha}_{n+1,i} = C_{3,i}\boldsymbol{\alpha}_{n,i} + C_{4,i}\lambda\mathbf{s}'_{n+1} \tag{A.5}$$

Making use of this equality alongside Eq. (19) leads to the following shape for the deviatoric shifted stress:

$$\mathbf{s}'_{n+1} = \left(1 + 2\overline{G}\lambda - \lambda^2 \sum_{i=1}^{m} C_{1,i}\right)^{-1} \left(\mathbf{s}'^{\text{TR}}_{n+1} + \lambda \sum_{i=1}^{m} C_{2,i}\boldsymbol{\alpha}_{n,i}\right) \tag{A.6}$$

To obtain $\tau_{y,n+1}$, Eq. (16) is hired reading:

$$\tau_{y,n+1} = \tau_{y,0} + \tau_{y,s}(1 - \exp(-\overline{b}\gamma_{n+1})) \quad \text{with} \quad \gamma_{n+1} = \gamma_n + \lambda \tag{A.7}$$

Employing the constitutive equality (23), the volumetric portion of the back stress is found as

$$\overline{p}_{n+1} = \sum_{i=1}^{m} \overline{p}_{n+1,i} \quad \text{with} \quad \overline{p}_{n+1,i} = C_{3,i}\overline{p}_{n,i} + \frac{2}{3}C_{4,i}\lambda\beta(\tau_{y,n+1} - \beta p'_{n+1}) \tag{A.8}$$

Having used Eqs. (23) and (A.8), one can compute the hydrostatic shifted stress in the next form:

$$p'_{n+1} = \frac{p'^{\text{TR}}_{n+1} - 2\beta\overline{K}\lambda\tau_{y,n+1} + \lambda \sum_{i=1}^{m} C_{2,i}\overline{p}_{n,i} + \frac{2}{3}\beta\lambda^2\tau_{y,n+1} \sum_{i=1}^{m} C_{1,i}}{1 - 2\beta^2\overline{K}\lambda + \frac{2}{3}\beta^2\lambda^2 \sum_{i=1}^{m} C_{1,i}} \tag{A.9}$$

The equalities (A.5)–(A.9) give rise to the updated values of $\mathbf{s}'_{n+1}$, p'_{n+1}, $\overline{p}_{n+1}$, and $\tau_{y,n+1}$. The only remained step to have them all known is the discrete plastic multiplier. For this purpose to happen, the yield function is utilized. This would bring us to the following nonlinear equality from which the plastic multiplier is computed:

$$\frac{|\mathbf{s}'^{\text{TR}}_{n+1} + \lambda \sum_{i=1}^{m} C_{2,i}\boldsymbol{\alpha}_{n,i}|^2}{(1 + 2\overline{G}\lambda - \lambda^2 \sum_{i=1}^{m} C_{1,i})^2} - 2\left[\tau_{y,n+1} - \frac{\left(p'^{\text{TR}}_{n+1} + \tau_{y,n+1}\left(\frac{2}{3}\beta\lambda^2 \sum_{i=1}^{m} C_{1,i} - 2\beta\overline{K}\lambda\right) + \lambda \sum_{i=1}^{m} C_{2,i}\overline{p}_n\right)}{\beta\left(1 - 2\beta^2\overline{K}\lambda + \frac{2}{3}\beta^2\lambda^2 \sum_{i=1}^{m} C_{1,i}\right)}\right]^2 = 0 \tag{A.10}$$

This massive equality is typically solved with Newton–Raphson method.

Appendix B. Forward Euler integration

Assuming that the stress state at time t_n lies on the yield surface, the discrete plastic multiplier is attained using Eq. (57). The total stress and its components are easily updated through constitutive Eqs. (7), (16), (20), (23), and the acquired λ. The following express them in detail:

$$\mathbf{s}'_{n+1} = \mathbf{s}'_n + 2G\Delta\mathbf{e} - 2\overline{G}\lambda\mathbf{s}'_n + \lambda \sum_{i=1}^{m} H_{\text{nl},i}\boldsymbol{\alpha}_{n,i} \tag{B.1}$$

$$p'_{n+1} = p'_n + K\Delta\varepsilon_v - 2\beta\lambda\overline{K}(\tau_{y,n} - \beta p'_n) + \sum_{i=1}^{m} H_{\text{nl},i}\lambda\overline{p}_n \tag{B.2}$$

$$\tau_{y,n+1} = \tau_{y,0} + \tau_{y,s}(1 - \exp(-\overline{b}\gamma_{n+1})) \quad \text{with} \quad \gamma_{n+1} = \gamma_n + \lambda \tag{B.3}$$

$$\overline{p}_{n+1,i} = \overline{p}_{n,i} + \frac{2}{3}H_{\text{kin},i}\lambda\beta(\tau_{y,n} - \beta p'_n) - \lambda H_{\text{nl},i}\overline{p}_{n,i} \tag{B.4}$$

$$\boldsymbol{\alpha}_{n+1} = \boldsymbol{\alpha}_n + \Delta\boldsymbol{\alpha}_{n+1} \quad \text{with} \quad \Delta\boldsymbol{\alpha}_{n+1} = \sum_{i=1}^{m} (H_{\text{kin},i}\Delta\mathbf{e}^{\text{p}} - H_{\text{nl},i}\lambda\boldsymbol{\alpha}_{n,i}) \tag{B.5}$$

Let's not forget that in this scheme the consistency condition is not automatically held. To impose the consistency a corrector vector is added to the deviatoric shifted stress in the direction normal to the yield surface. The correcting vector, $a_{\text{f}}\mathbf{n}_{n+1}$, is calculated through

$$F(\mathbf{s}'_{n+1} + a_{\text{f}}\mathbf{n}_{n+1}, \quad \tau_{y,n+1} - \beta p'_{n+1}) = 0 \quad \text{with} \quad \mathbf{n}_{n+1} = \frac{\mathbf{s}'_{n+1}}{\|\mathbf{s}'_{n+1}\|}$$

$$a_{\text{f}} = \sqrt{(\mathbf{n}^{\text{T}}_{n+1}\mathbf{s}'_{n+1})^2 - \|\mathbf{s}'_{n+1}\|^2 + 2(\tau_{y,n+1} - \beta p'_{n+1})^2} - \mathbf{n}^{\text{T}}_{n+1}\mathbf{s}'_{n+1} \tag{B.6}$$

Appendix C. Consistent tangent operator of the hybrid integration HXB

As discussed in Section 7, the components of Eq. (127) are needed in order to obtain the tangent modulus. What follows is the brief presentation of the required relationships.

The derivative of $\mathbf{s}'_{n+1}$ with respect to $\mathbf{e}_{n+1}$ is calculated using Eq. (59) together with Eqs. (50) and (52) reading

$$\frac{\partial \mathbf{s}'_{n+1}}{\partial \mathbf{e}_{n+1}} = \frac{1}{X_{n+1}^0}\frac{\partial \mathbf{X}_{n+1}^s}{\partial \mathbf{e}_{n+1}} - \frac{\mathbf{X}_{n+1}^s}{(X_{n+1}^0)^2}\frac{\partial X_{n+1}^0}{\partial \mathbf{e}_{n+1}} \tag{C.1}$$

$$\frac{\partial \mathbf{X}_{n+1}^s}{\partial \mathbf{e}_{n+1}} = (\Delta\hat{\boldsymbol{\mu}}^{\mathrm{T}}\mathbf{X}_n^s)\Delta\hat{\boldsymbol{\mu}}\left(\frac{\partial a_n}{\partial \mathbf{e}_{n+1}}\right)^{\mathrm{T}} + X_n^{\mathrm{R}}\Delta\hat{\boldsymbol{\mu}}\left(\frac{\partial b_n}{\partial \mathbf{e}_{n+1}}\right)^{\mathrm{T}} + (a_n-1)\Delta\hat{\boldsymbol{\mu}}\left[\frac{\partial\Delta\hat{\boldsymbol{\mu}}}{\partial \mathbf{e}_{n+1}}\mathbf{X}_n^s\right]^{\mathrm{T}} + ((a_n-1)(\Delta\hat{\boldsymbol{\mu}}^{\mathrm{T}}\mathbf{X}_n^s)+b_nX_n^{\mathrm{R}})\frac{\partial\Delta\hat{\boldsymbol{\mu}}}{\partial \mathbf{e}_{n+1}} \tag{C.2}$$

$$\frac{\partial X_{n+1}^0}{\partial \mathbf{e}_{n+1}} = \frac{1}{R_{n+1}}\frac{\partial X_{n+1}^{\mathrm{R}}}{\partial \mathbf{e}_{n+1}} + \frac{X_{n+1}^{\mathrm{R}}}{R_{n+1}^2}\frac{\partial R_{n+1}}{\partial \mathbf{e}_{n+1}} \tag{C.3}$$

$$\frac{\partial X_{n+1}^{\mathrm{R}}}{\partial \mathbf{e}_{n+1}} = (\Delta\hat{\boldsymbol{\mu}}^{\mathrm{T}}\mathbf{X}_n^s)\frac{\partial b_n}{\partial \mathbf{e}_{n+1}} + b_n\frac{\partial\Delta\hat{\boldsymbol{\mu}}}{\partial \mathbf{e}_{n+1}}\mathbf{X}_n^s + X_n^{\mathrm{R}}\frac{\partial a_n}{\partial \mathbf{e}_{n+1}} \tag{C.4}$$

The derivatives in Eqs. (C.2)–(C.4) are attained through Eqs. (53), (54), and (25):

$$\frac{\partial a_n}{\partial \mathbf{e}_{n+1}} = \frac{2G}{R_n}\sinh\left(\frac{2G}{R_n}\|\Delta\boldsymbol{\mu}\|\right)\frac{\partial\|\Delta\boldsymbol{\mu}\|}{\partial \mathbf{e}_{n+1}} \quad \text{and} \quad \frac{\partial b_n}{\partial \mathbf{e}_{n+1}} = \frac{2G}{R_n}\cosh\left(\frac{2G}{R_n}\|\Delta\boldsymbol{\mu}\|\right)\frac{\partial\|\Delta\boldsymbol{\mu}\|}{\partial \mathbf{e}_{n+1}} \tag{C.5}$$

$$\frac{\partial\|\Delta\boldsymbol{\mu}\|}{\partial \mathbf{e}_{n+1}} = \left[\mathbb{I} + \frac{1}{2G}\left(\sum_{i=1}^{m}H_{\mathrm{nl},i}\boldsymbol{\alpha}_{n,i}\right)\left(\frac{\partial\lambda^{\mathrm{ex}}}{\partial \mathbf{e}_{n+1}}\right)^{\mathrm{T}}\right]\Delta\hat{\boldsymbol{\mu}} \quad \text{and} \quad \frac{\partial\Delta\hat{\boldsymbol{\mu}}}{\partial \mathbf{e}_{n+1}} = \left[\frac{\partial\Delta\boldsymbol{\mu}}{\partial \mathbf{e}_{n+1}} - \frac{\Delta\boldsymbol{\mu}}{\|\Delta\boldsymbol{\mu}\|}\left(\frac{\partial\Delta\boldsymbol{\mu}}{\partial \mathbf{e}_{n+1}}\Delta\hat{\boldsymbol{\mu}}\right)^{\mathrm{T}}\right] \tag{C.6}$$

$$\frac{\partial R_{n+1}}{\partial \mathbf{e}_{n+1}} = \sqrt{2}\frac{\partial\tau_{y,n+1}}{\partial \mathbf{e}_{n+1}} - \sqrt{2}\beta\frac{\partial p'_{n+1}}{\partial \mathbf{e}_{n+1}} \tag{C.7}$$

Referring to Eq. (57), $\partial\lambda^{\mathrm{ex}}/\partial \mathbf{e}_{n+1}$ is computed as

$$\frac{\partial\lambda^{\mathrm{ex}}}{\partial \mathbf{e}_{n+1}} = \frac{2G\mathbf{s}'_n}{2(\overline{G}+\beta^2\overline{K})R_n^2 + \sqrt{2}R_n\left[\overline{b}(\tau_{y,0}+\tau_{y,s}-\tau_{y,n})-\beta\sum_{i=1}^{m}H_{\mathrm{nl},i}\overline{p}_{n,i}\right] - \mathbf{s}_n^T\sum_{i=1}^{m}H_{\mathrm{nl},i}\boldsymbol{\alpha}_{n,i}} \tag{C.8}$$

The derivative of $\mathbf{s}'_{n+1}$ with respect to $\varepsilon_{v,n+1}$ is also calculated utilizing Eq. (59) along with Eqs. (50) and (52) as

$$\frac{\partial \mathbf{s}'_{n+1}}{\partial \varepsilon_{v,n+1}} = \frac{1}{X_{n+1}^0}\frac{\partial \mathbf{X}_{n+1}^s}{\partial \varepsilon_{v,n+1}} - \frac{\mathbf{X}_{n+1}^s}{(X_{n+1}^0)^2}\frac{\partial X_{n+1}^0}{\partial \varepsilon_{v,n+1}} \tag{C.9}$$

$$\frac{\partial \mathbf{X}_{n+1}^s}{\partial \varepsilon_{v,n+1}} = (\Delta\hat{\boldsymbol{\mu}}^{\mathrm{T}}\mathbf{X}_n^s)\Delta\hat{\boldsymbol{\mu}}\frac{\partial a_n}{\partial \varepsilon_{v,n+1}} + X_n^{\mathrm{R}}\Delta\hat{\boldsymbol{\mu}}\frac{\partial b_n}{\partial \varepsilon_{v,n+1}} + (a_n-1)\frac{\partial\Delta\hat{\boldsymbol{\mu}}}{\partial \varepsilon_{v,n+1}}(\mathbf{X}_n^s)^{\mathrm{T}}\Delta\hat{\boldsymbol{\mu}} + ((a_n-1)(\Delta\hat{\boldsymbol{\mu}}^{\mathrm{T}}\mathbf{X}_n^s)+b_nX_n^{\mathrm{R}})\frac{\partial\Delta\hat{\boldsymbol{\mu}}}{\partial \varepsilon_{v,n+1}} \tag{C.10}$$

$$\frac{\partial X_{n+1}^0}{\partial \varepsilon_{v,n+1}} = \frac{1}{R_{n+1}}\frac{\partial X_{n+1}^{\mathrm{R}}}{\partial \varepsilon_{v,n+1}} + \frac{X_{n+1}^{\mathrm{R}}}{R_{n+1}^2}\frac{\partial R_{n+1}}{\partial \varepsilon_{v,n+1}} \tag{C.11}$$

$$\frac{\partial X_{n+1}^{\mathrm{R}}}{\partial \varepsilon_{v,n+1}} = (\Delta\hat{\boldsymbol{\mu}}^{\mathrm{T}}\mathbf{X}_n^s)\frac{\partial b_n}{\partial \varepsilon_{v,n+1}} + b_n\left(\frac{\partial\Delta\hat{\boldsymbol{\mu}}}{\partial \varepsilon_{v,n+1}}\right)^{\mathrm{T}}\mathbf{X}_n^s + X_n^{\mathrm{R}}\frac{\partial a_n}{\partial \varepsilon_{v,n+1}} \tag{C.12}$$

Using Eqs. (53), (54), (57) and (25) one can achieve

$$\frac{\partial a_n}{\partial \varepsilon_{v,n+1}} = \frac{2G}{R_n}\sin h\left(\frac{2G}{R_n}\|\Delta\boldsymbol{\mu}\|\right)\frac{\partial\|\Delta\boldsymbol{\mu}\|}{\partial \varepsilon_{v,n+1}} \quad \& \quad \frac{\partial b_n}{\partial \varepsilon_{v,n+1}} = \frac{2G}{R_n}\cos h\left(\frac{2G}{R_n}\|\Delta\boldsymbol{\mu}\|\right)\frac{\partial\|\Delta\boldsymbol{\mu}\|}{\partial \varepsilon_{v,n+1}} \tag{C.13}$$

$$\frac{\partial\|\Delta\boldsymbol{\mu}\|}{\partial \varepsilon_{v,n+1}} = \left[\frac{1}{2G}\left(\sum_{i=1}^{m}H_{\mathrm{nl},i}\boldsymbol{\alpha}_{n,i}\right)\frac{\partial\lambda^{\mathrm{ex}}}{\partial \varepsilon_{v,n+1}}\right]^{\mathrm{T}}\Delta\hat{\boldsymbol{\mu}} \quad \& \quad \frac{\partial\Delta\hat{\boldsymbol{\mu}}}{\partial \varepsilon_{v,n+1}} = \frac{1}{\|\Delta\boldsymbol{\mu}\|}\left[\frac{\partial\Delta\boldsymbol{\mu}}{\partial \varepsilon_{v,n+1}} - \left(\left(\frac{\partial\Delta\boldsymbol{\mu}}{\partial \varepsilon_{v,n+1}}\right)^{\mathrm{T}}\Delta\hat{\boldsymbol{\mu}}\right)\frac{\Delta\boldsymbol{\mu}}{\|\Delta\boldsymbol{\mu}\|}\right] \tag{C.14}$$

$$\frac{\partial R_{n+1}}{\partial \varepsilon_{v,n+1}} = \sqrt{2}\frac{\partial\tau_{y,n+1}}{\partial \varepsilon_{v,n+1}} - \sqrt{2}\beta\frac{\partial p'_{n+1}}{\partial \varepsilon_{v,n+1}} \tag{C.15}$$

$$\frac{\partial\lambda^{\mathrm{ex}}}{\partial \varepsilon_{v,n+1}} = \frac{\sqrt{2}\beta KR_n}{2(\overline{G}+\beta^2\overline{K})R_n^2 + \sqrt{2}R_n\left[\overline{b}(\tau_{y,0}+\tau_{y,s}-\tau_{y,n})-\beta\sum_{i=1}^{m}H_{\mathrm{nl},i}\overline{p}_{n,i}\right] - \mathbf{s}_n^T\sum_{i=1}^{m}H_{\mathrm{nl},i}\boldsymbol{\alpha}_{n,i}} \tag{C.16}$$

Furthermore, $\partial\boldsymbol{\alpha}_{n+1}/\partial \mathbf{e}_{n+1}$ and $\partial\boldsymbol{\alpha}_{n+1}/\partial\varepsilon_{v,n+1}$ are also calculated using Eqs. (63)–(65) as

$$\frac{\partial\boldsymbol{\alpha}_{n+1}}{\partial \mathbf{e}_{n+1}} = \sum_{i=1}^{m}\left(\left(\frac{4+\overline{\lambda}H_{\mathrm{nl},i}^2(1-\overline{\lambda})-2H_{\mathrm{nl},i}}{(2+\overline{\lambda}H_{\mathrm{nl},i})^2}\right)\boldsymbol{\alpha}_{n,i}\left(\frac{\partial\overline{\lambda}}{\partial \mathbf{e}_{n+1}}\right)^{\mathrm{T}} + \frac{2H_{\mathrm{kin},i}}{2+\overline{\lambda}H_{\mathrm{nl},i}}\frac{\partial\Delta\mathbf{e}^{\mathrm{p}}}{\partial \mathbf{e}_{n+1}} - \frac{2H_{\mathrm{kin},i}H_{\mathrm{nl},i}}{(2+\overline{\lambda}H_{\mathrm{nl},i})^2}\Delta\mathbf{e}^{\mathrm{p}}\left(\frac{\partial\overline{\lambda}}{\partial \mathbf{e}_{n+1}}\right)^{\mathrm{T}}\right) \tag{C.17}$$

$$\frac{\partial \boldsymbol{\alpha}_{n+1}}{\partial \varepsilon_{v,n+1}} = \sum_{i=1}^{m} \left(\frac{-4H_{\mathrm{nl},i}}{(2+\overline{\lambda}H_{\mathrm{nl},i})^2}\left(\frac{\partial\overline{\lambda}}{\partial\varepsilon_{v,n+1}}\right)\boldsymbol{\alpha}_{n,i} + \frac{2H_{\mathrm{kin},i}}{2+\overline{\lambda}H_{\mathrm{nl},i}}\frac{\partial\Delta\mathbf{e}^{\mathrm{p}}}{\partial\varepsilon_{v,n+1}} - \frac{2H_{\mathrm{kin},i}H_{\mathrm{nl},i}}{(2+\overline{\lambda}H_{\mathrm{nl},i})^2\left(\frac{\partial\overline{\lambda}}{\partial\varepsilon_{v,n+1}}\right)}\Delta\mathbf{e}^{\mathrm{p}} \right) \tag{C.18}$$

Since $\tau_{y,n+1}$, p', $\overline{p}$, and R are all updated through Backward Euler relationships, one needs referring to some equations in Appendix A for obtaining their derivatives. Consequently, the derivatives of the defined factors $C_{j,i}$ with respect to $\mathbf{e}_{n+1}$ and $\varepsilon_{v,n+1}$ are required reading:

$$\frac{\partial C_{1,i}}{\partial \mathbf{e}_{n+1}} = \frac{-H_{\mathrm{kin},i}H_{\mathrm{nl},i}^2}{(1+\lambda^{\mathrm{im}}H_{\mathrm{nl},i})^2}\frac{\partial\lambda^{\mathrm{im}}}{\partial\mathbf{e}_{n+1}} \quad \text{and} \quad \frac{\partial C_{1,i}}{\partial\varepsilon_{v,n+1}} = \frac{-H_{\mathrm{kin},i}H_{\mathrm{nl},i}^2}{(1+\lambda^{\mathrm{im}}H_{\mathrm{nl},i})^2}\frac{\partial\lambda^{\mathrm{im}}}{\partial\varepsilon_{v,n+1}} \tag{C.19}$$

$$\frac{\partial C_{2,i}}{\partial \mathbf{e}_{n+1}} = \frac{-H_{\mathrm{nl},i}^2}{(1+\lambda^{\mathrm{im}}H_{\mathrm{nl},i})^2}\frac{\partial\lambda^{\mathrm{im}}}{\partial\mathbf{e}_{n+1}} \quad \text{and} \quad \frac{\partial C_{2,i}}{\partial\varepsilon_{v,n+1}} = \frac{-H_{\mathrm{nl},i}^2}{(1+\lambda^{\mathrm{im}}H_{\mathrm{nl},i})^2}\frac{\partial\lambda^{\mathrm{im}}}{\partial\varepsilon_{v,n+1}} \tag{C.20}$$

$$\frac{\partial C_{3,i}}{\partial \mathbf{e}_{n+1}} = \frac{-H_{\mathrm{nl},i}}{(1+\lambda^{\mathrm{im}}H_{\mathrm{nl},i})^2}\frac{\partial\lambda^{\mathrm{im}}}{\partial\mathbf{e}_{n+1}} \quad \text{and} \quad \frac{\partial C_{3,i}}{\partial\varepsilon_{v,n+1}} = \frac{-H_{\mathrm{nl},i}}{(1+\lambda^{\mathrm{im}}H_{\mathrm{nl},i})^2}\frac{\partial\lambda^{\mathrm{im}}}{\partial\varepsilon_{v,n+1}} \tag{C.21}$$

$$\frac{\partial C_{1,i}}{\partial \mathbf{e}_{n+1}} = \frac{-H_{\mathrm{kin},i}H_{\mathrm{nl},i}}{(1+\lambda^{\mathrm{im}}H_{\mathrm{nl},i})^2}\frac{\partial\lambda^{\mathrm{im}}}{\partial\mathbf{e}_{n+1}} \quad \text{and} \quad \frac{\partial C_{1,i}}{\partial\varepsilon_{v,n+1}} = \frac{-H_{\mathrm{kin},i}H_{\mathrm{nl},i}}{(1+\lambda^{\mathrm{im}}H_{\mathrm{nl},i})^2}\frac{\partial\lambda^{\mathrm{im}}}{\partial\varepsilon_{v,n+1}} \tag{C.22}$$

The following relationships are computed through Eqs. (A.1), (A.7) and (A.8):

$$\frac{\partial \mathbf{s}'^{\mathrm{TR}}_{n+1}}{\partial\mathbf{e}_{n+1}} = 2G\mathbb{I} \quad \text{and} \quad \frac{\partial\mathbf{s}'^{\mathrm{TR}}_{n+1}}{\partial\varepsilon_{v,n+1}} = 0 \quad \text{and} \quad \frac{\partial p'^{\mathrm{TR}}_{n+1}}{\partial\mathbf{e}_{n+1}} = 0 \quad \text{and} \quad \frac{\partial p'^{\mathrm{TR}}_{n+1}}{\partial\varepsilon_{v,n+1}} = K\mathbf{i} \tag{C.23}$$

$$\frac{\partial\tau_{y,n+1}}{\partial\mathbf{e}_{n+1}} = \tau_{y,s}\overline{b}\exp(-\overline{b}\gamma_{n+1})\frac{\partial\lambda^{\mathrm{im}}}{\partial\mathbf{e}_{n+1}} \quad \text{and} \quad \frac{\partial\tau_{y,n+1}}{\partial\varepsilon_{v,n+1}} = \tau_{y,s}\overline{b}\exp(-\overline{b}\gamma_{n+1})\frac{\partial\lambda^{\mathrm{im}}}{\partial\varepsilon_{v,n+1}} \tag{C.24}$$

$$\frac{\partial\overline{p}_{n+1}}{\partial\mathbf{e}_{n+1}} = \sum_{i=1}^{m}\frac{\partial\overline{p}_{n+1,i}}{\partial\mathbf{e}_{n+1}} \rightarrow \frac{\partial\overline{p}_{n+1,i}}{\partial\mathbf{e}_{n+1}} = \overline{p}_{n,i}\frac{\partial C_{3,i}}{\partial\mathbf{e}_{n+1}} + \frac{\sqrt{2}}{3}\beta R_{n+1}\left(\lambda^{\mathrm{im}}\frac{\partial C_{4,i}}{\partial\mathbf{e}_{n+1}} + C_{4,i}\frac{\partial\lambda^{\mathrm{im}}}{\partial\mathbf{e}_{n+1}}\right) + \frac{2}{3}\beta C_{4,i}\lambda^{\mathrm{im}}\left(\frac{\partial\tau_{y,n+1}}{\partial\mathbf{e}_{n+1}} - \beta\frac{\partial p'_{n+1}}{\partial\mathbf{e}_{n+1}}\right) \tag{C.25}$$

Substituting $\partial/\partial\varepsilon_{v,n+1}$ for $\partial/\partial\mathbf{e}_{n+1}$ in the preceding equation gives the $\partial\overline{p}_{n+1}/\partial\varepsilon_{v,n+1}$. In addition, $\partial p'_{n+1}/\partial\mathbf{e}_{n+1}$ and $\partial p'_{n+1}/\partial\varepsilon_{v,n+1}$ are acquired via Eq. (A.9) in the following form where V and W, respectively, represent the numerator and denominator of Eq. (A.9) for the sake of simplicity:

$$p'_{n+1} = \frac{V}{W} \rightarrow \frac{\partial p'_{n+1}}{\partial\mathbf{e}_{n+1}} = \frac{(\partial V/\partial\mathbf{e}_{n+1})W-(\partial W/\partial\mathbf{e}_{n+1})V}{W^2} \quad \text{and} \quad \frac{\partial p'_{n+1}}{\partial\varepsilon_{v,n+1}} = \frac{(\partial V/\partial\varepsilon_{v,n+1})W-(\partial W/\partial\varepsilon_{v,n+1})V}{W^2} \tag{C.26}$$

$$\frac{\partial V}{\partial\mathbf{e}_{n+1}} = \left(\frac{4}{3}\beta\lambda^{\mathrm{im}}\tau_{y,n+1}\sum_{i=1}^{m}C_{1,i} - 2\beta\overline{K}\tau_{y,n+1} + \sum_{i=1}^{m}C_{2,i}\overline{p}_{n,i}\right)\frac{\partial\lambda^{\mathrm{im}}}{\partial\mathbf{e}_{n+1}} + \left(\frac{2}{3}\beta(\lambda^{\mathrm{im}})^2\sum_{i=1}^{m}C_{1,i} - 2\beta\lambda^{\mathrm{im}}\overline{K}\right)\frac{\partial\tau_{y,n+1}}{\partial\mathbf{e}_{n+1}}$$
$$+ \lambda^{\mathrm{im}}\sum_{i=1}^{m}\frac{\partial C_{2,i}}{\partial\mathbf{e}_{n+1}}\overline{p}_{n,i} + \frac{2}{3}\beta(\lambda^{\mathrm{im}})^2\tau_{y,n+1}\sum_{i=1}^{m}\frac{\partial C_{1,i}}{\partial\mathbf{e}_{n+1}} \tag{C.27}$$

$$\frac{\partial W}{\partial\mathbf{e}_{n+1}} = -2\beta^2\left(\overline{K} - \frac{2}{3}\lambda^{\mathrm{im}}\sum_{i=1}^{m}C_{1,i}\right)\frac{\partial\lambda^{\mathrm{im}}}{\partial\mathbf{e}_{n+1}} + \frac{2}{3}\beta^2(\lambda^{\mathrm{im}})^2\sum_{i=1}^{m}\frac{\partial C_{1,i}}{\partial\mathbf{e}_{n+1}} \tag{C.28}$$

Here, $\partial V/\partial\varepsilon_{v,n+1}$ and $(\partial W/\partial\varepsilon_{v,n+1})$ are easily obtained the same as Eqs. (C.27) and (C.28) only by replacing $\partial/\partial\mathbf{e}_{n+1}$ with $\partial/\partial\varepsilon_{v,n+1}$ along with adding the term $\partial p'^{\mathrm{TR}}_{n+1}/\partial\varepsilon_{v,n+1}$ to the acquired relation for $\partial V/\partial\varepsilon_{v,n+1}$. Note that, in the recent relationships λ^{im} is obtained via Eq. (A.10). Moreover, $\partial\lambda^{\mathrm{im}}/\partial\mathbf{e}_{n+1}$ and $\partial\lambda^{\mathrm{im}}/\partial\varepsilon_{v,n+1}$ are secured by taking the derivatives of Eq. (A.10) with respect to $\mathbf{e}_{n+1}$ and $\varepsilon_{v,n+1}$ using the same procedure as above. This will lead to two separate massive nonlinear equations for $\partial\lambda^{\mathrm{im}}/\partial\mathbf{e}_{n+1}$ and $\partial\lambda^{\mathrm{im}}/\partial\varepsilon_{v,n+1}$, which are solved by means of a numerical solver like the Newton–Raphson method.

References

[1] Jones RM. Deformation theory of plasticity. Bull Ridge Corp; 2009.
[2] Wilkins ML. Calculation of elastic–plastic flow. Methods Comput Phys, vol.3. Acad. Press; 1963.
[3] Rice JR, Tracey DM. Computational fracture mechanics. Proc Symp Numer Meth Struct Mech 1973;585.
[4] Krieg RD, Key SW. Implementation of a time dependent plasticity theory into structural computer programs. In: Stricklin JA, Saczalski KJ, editors. Constitutive equations in viscoplasticity: computational and engineering aspects, AMD-20. New York: ASME; 1976. p. 125–37.
[5] Krieg RD, Krieg DB. Accuracies of numerical solution methods for the elastic-perfectly plastic model. J Press Vessel Tech Trans ASME 1977;99:510–5.
[6] Schreyer HL, Kulak RL, Kramer JM. Accurate numerical solutions for elastic–plastic models. J Press Vessel Tech ASME 1979;101.
[7] Yoder PJ, Whirley RG. On the numerical implementations of elastoplastic models. J Appl Mech ASME 1984;51:283–8.
[8] Ortiz M, Popov EP. Accuracy and stability of integration algorithms for elasto-plastic constitutive relations,. Int J Numer Meth Eng 1985;21:1561–76.
[9] Nagtegaal JC. On the implementation of inelastic constitutive equations with special reference to large deformation problems. Comput Meth Appl Mech Eng 1982;33:469–84.
[10] Simo JC, Taylor RL. Consistent tangent operators for rate-independent elasto-plasticity. Comput Meth Appl Mech Eng 1985;48:101–18.
[11] Simo JC, Taylor RL. A return mapping algorithm for plane stress elasto-plasticity. Int J Numer Meth Eng 1986;22:649–70.

[12] Dodds RH. Numerical techniques for plasticity computations in finite element analysis. Comput Struct 1987;26(5):767–79.

[13] Loret B, Prevost JH. Accurate numerical solutions for Drucker–Prager elastic-plastic models. Comput Meth Appl Mech Eng 1986;54:259–77.

[14] Runesson K, Sture S, Willam K. Integration in computational plasticity. Comput Struct 1988;30(1/2):119–30.

[15] Sloan SW, Booker JR. Integration of Tresca and Mohr–Coulomb constitutive relations in plane strain elasto-plasticity. Int J Numer Meth Eng 1992;33:163–196.

[16] Genna F, Pandolfi A. Accurate numerical integration of Drucker–Prager's constitutive equations. Mecc 1994;29:239–60.

[17] Hopperstad OS, Remseth S. A return mapping algorithm for a class of cyclic plasticity models. Int J Numer Meth Eng 1995;38:549–64.

[18] Wei Z, Perić D, Owen DRJ. Consistent linearization for the exact stress update of Prandtl–Reuss non-hardening elasto-plastic models. Int J Numer Meth Eng 1996;39:1219–35.

[19] Kobayashi M, Ohno N. Implementation of cyclic plasticity models based on a general form of kinematic hardening. Int J Numer Meth Eng 2002;53:2217–38.

[20] Kobayashi M, Mukai M, Takahashi H, Ohno N, Kawakami T, Ishikawa T. Implicit integration and consistent tangent modulus of a time-dependent non-unified constitutive model. Int J Numer Meth Eng 2003;58:1523–43.

[21] Clausen J, Damkilde L, Anderson L. Efficient return algorithms for associated plasticity with multiple yield planes. Int J Numer Meth Eng 2006;66:1036–59.

[22] Kan QH, Kang G, Zhang J. A unified visco-plastic constitutive model for uniaxial time-dependent ratchetting and its finite element implementation. Theor Appl Fract Mech 2007;47:133–44.

[23] Coombs WM, Crouch RS, Augarde CE. Reuleaux plasticity: analytical backward Euler stress integration and consistent tangent. Comput Meth Appl Mech Eng 2010;199:1733–43.

[24] Hong H-K, Liu C-S. Internal symmetry in bilinear elastoplasticity. Int J Non-Linear Mech 1999;34:279–88.

[25] Hong H-K, Liu C-S. Internal symmetry in the constitutive model of perfect elasto-plasticity. Int J Non-Linear Mech 2000;35:447–66.

[26] Hong H-K, Liu C-S. Lorentz group on Minkowski spacetime for construction of the two basic principles of plasticity. Int J Non-Linear Mech 2001;36:679–86.

[27] Auricchio F, Beirão da Veiga L. On a new integration scheme for von-Mises plasticity with linear hardening. Int J Numer Meth Eng 2003;56:1375–96.

[28] Artioli E, Auricchio F, Beirão da Veiga L. Integration schemes for von-Mises plasticity models based on exponential maps: numerical investigations and theoretical considerations. Int J Numer Meth Eng 2005;64:1133–65.

[29] Liu C-S. Symmetry groups and the pseudo-Riemann spacetimes for mixed-hardening elasto-plasticity. Int J Solids Struct 2003;40:251–69.

[30] Liu C-S. A consistent numerical scheme for the von-Mises mixed-hardening constitutive equations. Int J Plast 2004;20:663–704.

[31] Liu C-S. Internal symmetry groups for the Drucker–Prager material model of plasticity and numerical integrating methods. Int J Solids Struct 2004;41:3771–3791.

[32] Artioli E, Auricchio F, Beirão da Veiga L. A novel 'optimal' exponential-based integration algorithm for von-Mises plasticity with linear hardening: theoretical analysis on yield consistency, accuracy, convergence and numerical investigations. Int J Numer Meth Eng 2006;67(4):449–98.

[33] Artioli E, Auricchio F, Beirão da Veiga L. Second-order accurate integration algorithms for von-Mises plasticity with a nonlinear kinematic hardening mechanism. Comput Meth Appl Mech Eng 2007;196:1827–46.

[34] Rezaiee-Pajand M, Nasirai C. Accurate integration scheme for von-Mises plasticity with mixed-hardening based on exponential maps. Eng Comput 2007;24(6):608–35.

[35] Rezaiee-Pajand M, Nasirai C. On the integration schemes for Drucker–Prager's elasto-plastic models based on exponential maps. Int J Numer Meth Eng 2008;74:799–826.

[36] Rezaiee-Pajand M, Nasirai C, Sharifian M. Application of exponential-based methods in integrating the constitutive equations with multicomponent kinematic hardening. J Eng Mech ASCE 2010;136(12):1502–18.

[37] Rezaiee-Pajand M, Nasirai C, Sharifian M. Integration of nonlinear mixed hardening models. Multidiscip Model Mater Struct 2011;7(3):266–305.

[38] Sloan SW, Abbo AJ, Sheng D. Refined explicit integration of elasto-plastic models with automatic error control. Eng Comput 2001;18(1/2):121–54.

[39] Solowski WT, Gallipoli D. Explicit integration with error control for the Barcelona basic model, Part II: algorithm efficiency and accuracy. Comput Geotech 2010;37:68–81.

[40] Wallin M, Ristinmaa M. Accurate stress updating algorithm based on constant strain rate assumption. Comput Meth Appl Mech Eng 2001;190:5583–601.

[41] Wallin M, Ristinmaa M. An alternative method for the integration of continuum damage evolution laws. Comput Mech 2008;41:347–59.

[42] Szabó L. A semi-analytical integration method for J2 flow theory of plasticity with linear isotropic hardening. Comput Meth Appl Mech Eng 2009;198:2151–2166.

[43] Kossa A, Szabó L. Exact integration of the von Mises elastoplasticity model with combined linear isotropic-kinematic hardening. Int J Plast 2009;25:1083–106.

[44] Rezaiee-Pajand M, Sharifian M. A novel formulation for integrating nonlinear kinematic hardening Drucker–Prager's yield condition. Eur J Mech A/Solids 2012;31:163–78.

[45] Drucker DC, Prager W. Soil mechanics and plastic analysis or limit design. Quart Appl Math 1952;10:157–65.

[46] Chaboche, J.L., Dang-Van, K., Cordier, G., Modelization of strain memory effect on the cyclic hardening of 316 stainless steel. In: Proceedings of the translations of 5th international conference on structural mechanics in reactor technology, No. Div L in 11/3, Berlin; 1979.

[47] Chaboche JL. Time-independent constitutive theories for cyclic plasticity. Int J Plast 1986;2:149–88.

[48] Chaboche JL. On some modifications of kinematic hardening to improve the description of ratcheting effects. Int J Plast 1991;7:661–78.

[49] Rezaiee-Pajand M, Sinaie S. On the calibration of the Chaboche hardening model and a modified hardening rule for uniaxial ratcheting prediction. Int J Solids Struct 2009;74:799–826.

[50] Rezaiee-Pajand M, Sharifian M, Sharifian M. Accurate and approximate integrations of Drucker–Prager plasticity with linear isotropic and kinematic hardening. Eur J Mech A/Solids 2011;30:345–61.

[51] de Souza Neto, E.A., Perić, D., Owen, D.R.J., Computational methods for plasticity: theory and applications, John Wiley and Sons, Ltd, 2008.

[52] Szabó L, Kossa A. A new exact integration method for the Drucker–Prager elastoplastic model with linear isotropic hardening. Int J Solids Struct 2012;49:170–90.

[53] Arregui IL, Alfrerdsson B. Elastic-plastic characterization of a high strength bainitic roller bearing steel–experiments and modeling. Int J Mech Sci 2010;52:1254–68.

[54] Ortiz M, Simo JC. An analysis of a new class of integration algorithms for elasto-plastic constitutive relations. Int J Numer Meth Eng 1986;23:353–66.

[55] Simo JC, Hughes TJR. Computational inelasticity. New York: Springer-Verlag; 1998.